

# Mechanistic Insight into Hydrocarbon Synthesis via CO<sub>2</sub> Hydrogenation on $\chi$ -Fe<sub>5</sub>C<sub>2</sub> Catalysts

Haozhi Wang, Xiaowa Nie,\* Yuan Liu, Michael J. Janik, Xiaopeng Han,\* Yida Deng, Wenbin Hu, Chunshan Song, and Xinwen Guo\*



Cite This: *ACS Appl. Mater. Interfaces* 2022, 14, 37637–37651



Read Online

ACCESS |

Metrics & More

Article Recommendations

Supporting Information

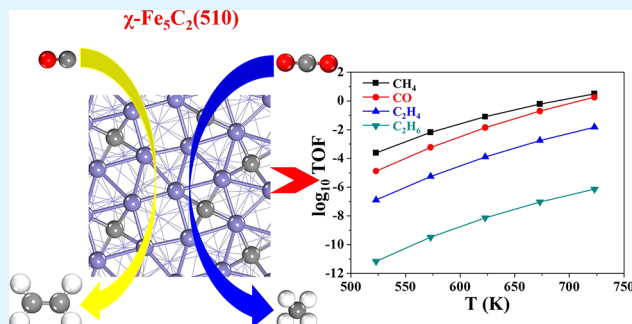
**ABSTRACT:** Converting CO<sub>2</sub> into value-added chemicals and fuels is one of the promising approaches to alleviate CO<sub>2</sub> emissions, reduce the dependence on nonrenewable energy resources, and minimize the negative environmental effect of fossil fuels. This work used density functional theory (DFT) calculations combined with microkinetic modeling to provide fundamental insight into the mechanisms of CO<sub>2</sub> hydrogenation to hydrocarbons over the iron carbide catalyst, with a focus on understanding the energetically favorable pathways and kinetic controlling factors for selective hydrocarbon production. The crystal orbital Hamiltonian population analysis demonstrated that the transition states associated with O–H bond formation steps within the path are less stable than those of C–H bond formation, accounting for the observed higher barriers in O–H bond formation from DFT. Energetically favorable pathways for CO<sub>2</sub> hydrogenation to CH<sub>4</sub> and C<sub>2</sub>H<sub>4</sub> products were identified which go through an HCOO intermediate, while the CH\* species was found to be the key C<sub>1</sub> intermediate over  $\chi$ -Fe<sub>5</sub>C<sub>2</sub>(510). The microkinetic modeling results showed that the relative selectivity to CH<sub>4</sub> is higher than C<sub>2</sub>H<sub>4</sub> in CO<sub>2</sub> hydrogenation, but the trend is opposite under CO hydrogenation conditions. The major impact on C<sub>2</sub> hydrocarbon production is attributed to the high surface coverage of O\* from CO<sub>2</sub> conversion, which occupies crucial active sites and impedes C–C couplings to C<sub>2</sub> species over  $\chi$ -Fe<sub>5</sub>C<sub>2</sub>(510). The coexistence of iron oxide and carbide phases was proposed and the interfacial sites created between the two phases impact CO<sub>2</sub> surface chemistry. Adding potassium into the Fe<sub>5</sub>C<sub>2</sub> catalyst accelerates O\* removal from the carbide surface, enhances the stability of the iron carbide catalyst, thus, promotes C–C couplings to hydrocarbons.

**KEYWORDS:** carbon dioxide hydrogenation, hydrocarbons,  $\chi$ -Fe<sub>5</sub>C<sub>2</sub>, density functional theory, microkinetic modeling

## 1. INTRODUCTION

The increase of CO<sub>2</sub> concentration in the atmosphere has caused many problems such as the greenhouse effect, sea level rise, and ocean acidification.<sup>1</sup> Despite great efforts having been made over the last decades, CO<sub>2</sub> concentration control and efficient conversion remain challenging.<sup>2</sup> The catalytic hydrogenation of CO<sub>2</sub> using H<sub>2</sub> derived from renewable energy sources (such as solar, wind, and biomass) to produce hydrocarbons and higher oxygenates is an important research direction in the field of heterogeneous catalysis and CO<sub>2</sub> chemistry and has also become one of the promising approaches in energy storage.<sup>3–7</sup> The advances in energy-efficient CO<sub>2</sub> conversion can potentially alleviate CO<sub>2</sub> emissions, reduce the dependence on nonrenewable energy resources, and minimize the negative environmental effect from traditional fossil fuels.<sup>8–10</sup>

The performance of Fe-, Co- and Ni-based active metals catalysts in Fischer–Tropsch (F–T) synthesis has attracted extensive attention, as well as in the CO<sub>2</sub> hydrogenation to hydrocarbons.<sup>11</sup> Among them, the Fe catalyst is one of the



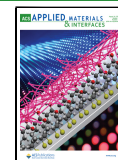
most promising components for CO<sub>2</sub> hydrogenation to C<sub>2</sub><sup>+</sup> hydrocarbon synthesis.<sup>12–16</sup> In addition, adding promoters (e.g., K and Mn),<sup>12,15–17</sup> using appropriate supports (e.g., Al<sub>2</sub>O<sub>3</sub> and SiO<sub>2</sub>),<sup>12,15,16</sup> or introducing other active components (e.g., Cu, Pd, Co, and Ni) are effective ways to regulate the catalytic performance of iron-based catalysts.<sup>18,19</sup>

Amoyal et al. researched the influence of K promoter on the CO<sub>2</sub> hydrogenation to liquid fuels over Fe catalyst and the spent catalysts were found to consist of both iron oxide and carbide components.<sup>20</sup> Visconti et al. found that metallic iron and iron oxides are active phases in the CO<sub>2</sub> hydrogenation over an iron-based F–T catalyst, while iron carbide species are conducive to the coupling of carbon–carbon bonds and the

Received: April 20, 2022

Accepted: July 29, 2022

Published: August 15, 2022



formation of the carbon chain, which is beneficial to the production of higher hydrocarbons.<sup>21</sup> Moreover, the iron carbide species can be oxidized during the reaction, leading to different selectivities to  $C_2^+$  hydrocarbons. Albrecht et al. detected some  $Fe_5C_2$  in the spent catalyst that used  $Fe_2O_3$  catalyst to convert  $CO_2$  into high hydrocarbons, indicating that the catalyst phase transition occurred during the reaction.<sup>5</sup> In our recent experimental works, a variety of carbides such as  $Fe_5C_2$  and  $Fe_3C$  were produced in the  $CO_2$  hydrogenation over an iron catalyst, indicating that there are complex phase changes in the reaction process.<sup>14,22,23</sup> Experimental results also suggested that the activity of  $Fe_3C$  for  $CO_2$  conversion to olefin is lower than that of  $Fe_5C_2$ .<sup>24,25</sup> In the experimental work by Zhang et al., the operando spectroscopic study was performed to investigate the structural transformation process of iron oxide catalysts under the condition of  $CO_2$  hydrogenation.<sup>26</sup> Different crystal forms of  $Fe_2O_3$  may lead to different phases of iron carbides, showing that the  $\alpha$ - $Fe_2O_3$  would be the precursor of  $\chi$ - $Fe_5C_2$ , while the formation of  $\theta$ - $Fe_3C$  requires a  $\gamma$ - $Fe_2O_3$  phase as the input catalyst under  $CO_2$  hydrogenation conditions. The results show that  $Fe_5C_2$  is an active species for  $C_2-C_4$  lower hydrocarbons formation while  $Fe_3C$  leads to the formation of  $C_5^+$  higher hydrocarbons. Although a number of experiments have investigated how to promote the catalytic activity and selectivity of hydrocarbon synthesis via hydrogenation of  $CO_2$  over iron-based catalysts, the active sites and functions of the various Fe species generated during the reaction are still unsolved to date because the reaction systems are very complicated and phase transformation of catalysts occurs along with  $CO_2$  reactions.

Recent theoretical studies on the hydrogenation of  $CO_2$  to hydrocarbons over iron-based catalysts show that the  $Fe_5C_2$  phase is easy to form, which is a crucial active iron species during  $CO_2$  transformation.<sup>17,22,26-30</sup> In F-T synthesis, the  $\chi$ - $Fe_5C_2$  is commonly considered to be the active phase for the coupling of carbon–carbon bonds and the formation of the carbon chain, which is believed to be responsible for the higher F-T activity.<sup>31-34</sup> Among the various exposed facets of  $\chi$ - $Fe_5C_2$ , the (510) facet was the most thermodynamically stable and accounted for the largest proportion of total surface area (34.9%) based on Wulff construction.<sup>35</sup> This result has been widely used to model the  $\chi$ - $Fe_5C_2$  catalyst in relevant theoretical studies.<sup>35-37</sup> Although the  $\chi$ - $Fe_5C_2$  is a highly proposed active species for FTS activity, which may be also active for  $CO_2$  hydrogenation, the  $CO_2$  hydrogenation condition is quite different from that of CO, and therefore, the catalytic properties and selectivities would be very different from the two reactants. The mechanism of CO hydrogenation to hydrocarbon over  $\chi$ - $Fe_5C_2$  catalysts was studied theoretically.<sup>34-39</sup> However, there are hardly any theoretical studies relevant to hydrocarbon synthesis via  $CO_2$  hydrogenation over  $\chi$ - $Fe_5C_2$  catalysts so far.

Identification of the actual active Fe species for hydrocarbon production from  $CO_2$  hydrogenation would be extremely difficult because phase transformation of iron catalysts occurs during the reaction, and multiple active phases may work together to consecutively catalyze  $CO_2$  conversion. However, a fundamental point of view on the function of  $Fe_5C_2$  species in  $CO_2$  reaction is very important because  $CO_2$  conversion paths may overlap, with some involved in F-T synthesis, where the  $\chi$ - $Fe_5C_2$  is considered to be the key active Fe species in C–C coupling and long-chain hydrocarbons formation.

In this paper, we investigate the pathways of  $CO_2$  hydrogenation to hydrocarbons over the  $\chi$ - $Fe_5C_2$ (510) surface using density functional theory (DFT) calculations, with a focus on identifying the mechanisms and key intermediates for the formation of  $CH_4$  and  $C_2H_4$  products. Combined with DFT, microkinetic modeling calculations were conducted to evaluate the relative selectivities of key products such as CO,  $CH_4$ ,  $C_2H_4$ , and  $C_2H_6$ . Furthermore, the comparisons between  $CO_2$  and CO hydrogenation properties were discussed to reveal key factors for the observed different selectivities from using these two reactants. The above calculated results of  $CO_2$  conversion mechanisms provide a design strategy for  $CO_2$  hydrogenation catalysts to hydrocarbon synthesis with highly selective.

## 2. COMPUTATIONAL DETAILS

The DFT calculations were performed by the Vienna ab-initio simulation package using the projector augmented wave potentials to deal with the ion cores interactions.<sup>40-44</sup> The Perdew–Burke–Ernzerhof functional under generalized gradient approximation level was adopted to calculate the electronic exchange and correlation energies.<sup>45</sup> The 400 eV cutoff energy and spin-polarized calculations were performed to capture the suitable magnetic properties of iron. A  $p(2 \times 1)$  supercell of  $\chi$ - $Fe_5C_2$ (510) containing three layers was constructed to model the iron carbide catalyst in this work (*Supporting Information* Figure S1). The bottom two layers atoms of  $\chi$ - $Fe_5C_2$ (510) were fixed, and all the atoms on the top layer were optimized until the force was reached. A gamma-point was used for surface calculations, and a  $3 \times 3 \times 1$   $k$ -mesh sampling with the Monkhorst–Pack scheme was also applied to test  $CO_2$  adsorption and initial hydrogenation energies to ensure the structural and energy convergence of calculations by gamma point. The results are provided in *Table S1*. The vacuum thickness of the slab was set to 12 Å to avoid interactions between repeating slabs.

The adsorption energy ( $E_{ads}$ ) of the surface species is calculated by *eq 1*

$$E_{ads} = E_{\text{species-surface}} - E_{\text{surface}} - E_{\text{species}} \quad (1)$$

where  $E_{\text{species-surface}}$  is the total energy of the adsorbed species with catalyst,  $E_{\text{surface}}$  and  $E_{\text{species}}$  represent the energy of the unoccupied surface and species in the gas phase, respectively. The climbing image nudged elastic band method was used to calculate the transition states.<sup>46</sup> The minimum energy path was examined by interpolating 6–8 images during the transition state search. All states involved in the reaction path were verified by the vibration frequency calculation, and each transition state was confirmed to have a single imaginary vibrational frequency along the reaction coordinate. Bader charge calculations<sup>47</sup> were performed to analyze the electron transfer properties via adsorbate–surface interactions.

The rate constants and equilibrium constants of surface reactions were calculated using the standard transition state theory.<sup>48,49</sup> For gas phase molecules, the translational, rotational, vibrational, and electronic partition functions were considered, while for surface intermediates and transition states, only the vibrational and electronic partition functions were included. The rate constants for forward and reverse reactions were calculated according to *eq 2*

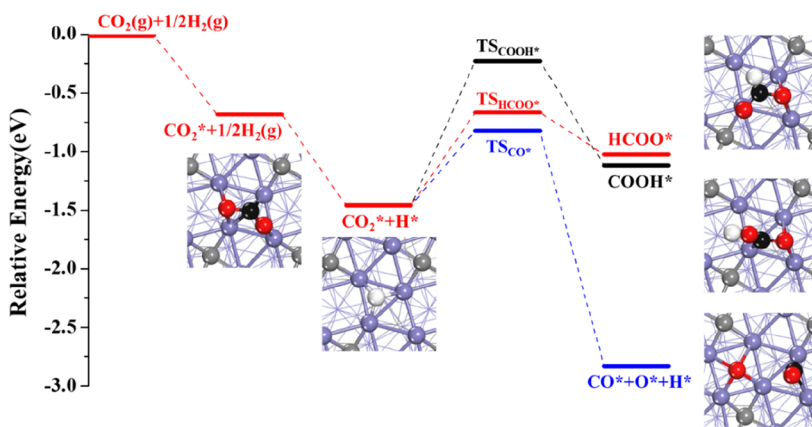


**Figure 1.** Energy profiles of the three possible pathways for  $\text{CO}_2$  initial conversions over the  $\chi\text{-Fe}_5\text{C}_2(510)$  surface. (Purple: Fe; black: C of adsorbates; red: O; white: H; and gray: C of  $\chi\text{-Fe}_5\text{C}_2$  catalyst).

$$k = \left( \frac{k_B T}{h} \right) \left( \frac{q^{\text{TS}}}{q^{\text{IS or FS}}} \right) e^{-\frac{E_a + \text{ZPE}}{k_B T}} \quad (2)$$

where  $k_B$ ,  $T$ ,  $h$ , ZPE, and  $E_a$  are Boltzmann constant, reaction temperature, Planck's constant, zero point energy (ZPE), and activation barrier calculated from DFT, respectively. The  $q^{\text{IS or FS}}$  and  $q^{\text{TS}}$  are harmonic vibrational partition functions for the initial (or final) and transition states, respectively. The vibrational partition functions were defined as eq 3

$$q = \prod_i \frac{1}{1 - e^{-hv_i/k_B T}} \quad (3)$$

where  $v_i$  is the vibrational frequency of each vibrational mode of intermediate and transition state calculated by DFT,  $i$  runs toward  $N$  and  $N - 1$  of initial (or final) and transition states, respectively. The thermodynamic equilibrium constant ( $K_{\text{eq}}$ ) is calculated by eq 4

$$K_{\text{eq}} = \frac{k_{\text{fwd}}}{k_{\text{rev}}} \quad (4)$$

Based on the pseudo-steady state hypothesis, the mean-field micro-kinetic modeling was applied to determine the reaction kinetics. This theoretical method for solving a system of the coupled ordinary differential equation describing the fractional surface coverages has been performed in various surface reactions.<sup>50</sup>

### 3. RESULTS AND DISCUSSION

**3.1. Adsorptions of Key Species.** The lattice parameter of the  $\text{Fe}_5\text{C}_2$  unit cell is given in Table S2, which is consistent with the results of previous research.<sup>30</sup> The optimized structure of the  $\chi\text{-Fe}_5\text{C}_2(510)$  surface is shown in Figure S1, with all possible adsorption sites marked out in the figure. There are two iron regions interlaced over the (510) surface, and the Fe atoms have been found to show strong interactions with adsorbates such as  $\text{CO}_2$  and CO in previous experimental and theoretical studies.<sup>51–53</sup> The top- and sub-layered carbon atoms are not active sites for adsorptions of surface species.

We first examined the adsorptions of molecules of  $\text{CO}_2$ ,  $\text{H}_2$ , CO,  $\text{CH}_4$ ,  $\text{C}_2\text{H}_4$ ,  $\text{C}_2\text{H}_6$ , and  $\text{H}_2\text{O}$  over the  $\chi\text{-Fe}_5\text{C}_2(510)$  surface because these species are reactants, intermediates, or products involved in the  $\text{CO}_2$  hydrogenation reaction. Figure S2 gives the optimized stable adsorption configuration of these molecules, which is consistent with the results of previous

studies.<sup>30</sup>  $\text{CO}_2$  was found to be adsorbed over the 3-fold hollow Fe site, which is known as the active site for  $\text{CO}_2$  activation on  $\chi\text{-Fe}_5\text{C}_2(510)$  via binding of C and O atoms to surface Fe. The calculated adsorption energy of  $\text{CO}_2$  is  $-0.68$  eV. Once the molecular  $\text{H}_2$  was placed onto the surface, it is readily dissociated into two atomic  $\text{H}^*$ , indicating a sufficient activation of  $\text{H}_2$  on  $\chi\text{-Fe}_5\text{C}_2(510)$ . The most stable adsorption site of atomic  $\text{H}^*$  is still the 3-fold hollow Fe site. The CO molecule can be stably adsorbed at the Fe-top site, and the adsorption energy is  $-2.12$  eV, close to the values obtained by Lu et al.<sup>38</sup> and Pham et al.<sup>35</sup> Water could be generated during  $\text{CO}_2$  conversion, and its adsorption stability can impact the efficacy of active sites and the stability of intermediates and may alter reaction pathways. On the  $\chi\text{-Fe}_5\text{C}_2(510)$  surface, it was found that the  $\text{H}_2\text{O}$  molecule prefers to adsorb on the top Fe site with a binding energy of  $-0.71$  eV, showing a moderate adsorption strength.  $\text{CH}_4$  is adsorbed at the top Fe site, and the adsorption energy is only  $-0.14$  eV, indicating a weak interaction between  $\text{CH}_4$  and the catalyst surface. For  $\text{C}_2\text{H}_4$ , the energetically favorable adsorption occurs on the 4-fold hollow Fe site via bonding of C atoms to surface Fe atom, and the adsorption energy was calculated to be  $-1.43$  eV.  $\text{C}_2\text{H}_6$  is a coordination saturated species with weak adsorption of  $\chi\text{-Fe}_5\text{C}_2(510)$  and binding energy close to zero. In general, the adsorption strength of CO and  $\text{C}_2\text{H}_4$  is relatively stronger, while  $\text{CO}_2$  and  $\text{H}_2\text{O}$  show moderate adsorption strength, and the adsorption of  $\text{CH}_4$  and  $\text{C}_2\text{H}_6$  is much weaker over the  $\chi\text{-Fe}_5\text{C}_2(510)$  surface.

**3.2.  $\text{CO}_2$  Hydrogenation Pathways.** The pathway commonly accepted for  $\text{CO}_2$  hydrogenation to  $\text{CH}_3\text{OH}$  synthesis over copper-based catalysts goes through a formate (HCOO) intermediate, while  $\text{CO}_2$  conversion to  $\text{CH}_3\text{OH}$  does not necessarily go through a CO intermediate.<sup>4,54–56</sup> As for hydrocarbon synthesis via  $\text{CO}_2$  hydrogenation over iron-based catalysts, the CO species was usually considered as the key intermediate, through which  $\text{CO}_2$  can be transformed to hydrocarbons through RWGS together with an FTS process. In Section 3.3, the microkinetic modeling study on  $\text{CO}_2$  hydrogenation and the activation barriers of many key intermediates in  $\text{CO}_2$  hydrogenation have been listed in Table 2. It can be observed that the barrier of CO desorption is  $2.12$  eV, while the barrier of  $\text{CO}^*$  hydrogenation into HCO\* and COH\* are  $0.84$  and  $0.91$  eV, respectively. Hence, the barrier energy of CO desorption is much higher than that of

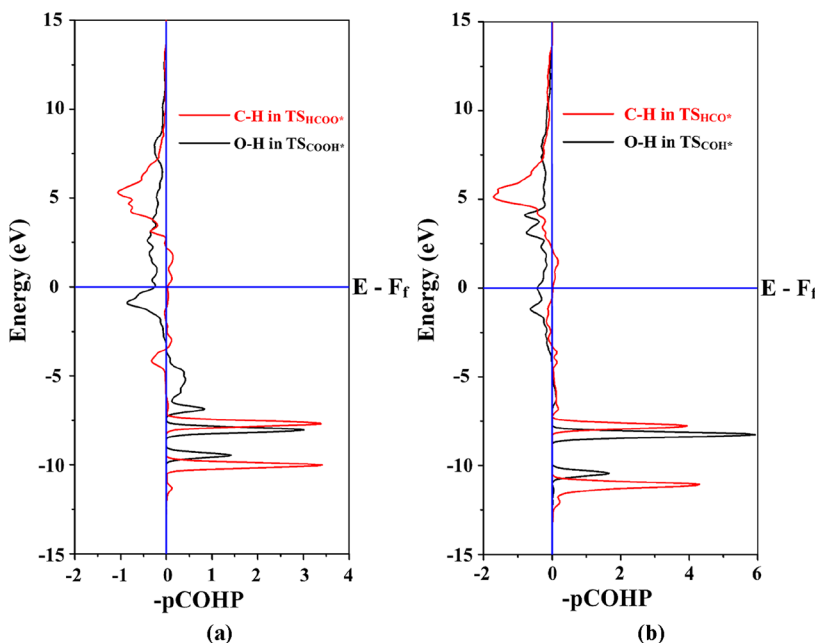


**Figure 2.** COHP for the interaction of C–H and O–H bonds in the transition states of (a) CO<sub>2</sub> and (b) CO hydrogenation over  $\chi\text{-Fe}_5\text{C}_2(510)$ .

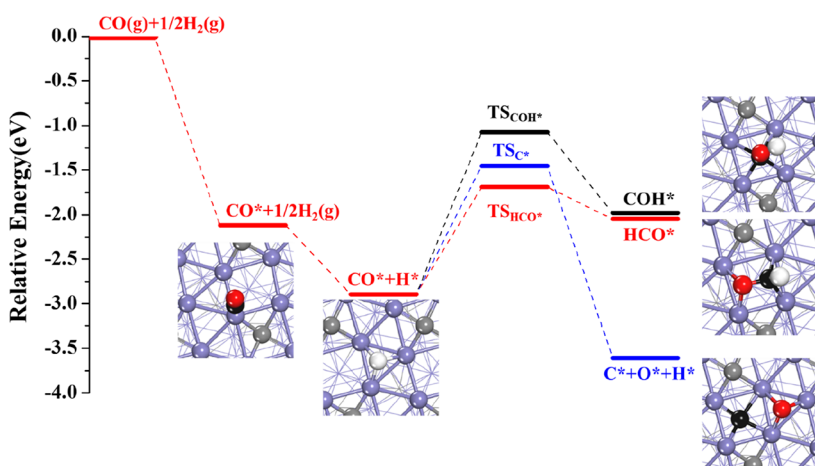


**Figure 3.** Energy profiles of the three possible pathways for CO conversion over the  $\chi\text{-Fe}_5\text{C}_2(510)$  surface. (Purple: Fe; black: C of adsorbates; red: O; white: H; gray: C of  $\chi\text{-Fe}_5\text{C}_2$  catalyst).

CO\* conversion to COH\* and HCO\*, indicating that CO is not the main product.

**3.2.1. CO<sub>2</sub> Initial Conversion over  $\chi\text{-Fe}_5\text{C}_2(510)$ .** In this work, three possible pathways were examined for the initial conversion of CO<sub>2</sub> over the  $\chi\text{-Fe}_5\text{C}_2(510)$  surface, including CO<sub>2</sub> dissociation to CO and CO<sub>2</sub> hydrogenation to COOH or HCOO intermediate. The energy diagrams associated with these pathways are illustrated in Figure 1. Optimized structures and key structural parameters of all states are provided in Figure S3 and Tables S3–S5. The formation of COOH\* is energetically unfavorable due to the high activation barrier of 1.23 eV and the low endothermic reaction energy of 0.34 eV. Even though the COOH\* can form on the  $\chi\text{-Fe}_5\text{C}_2(510)$  surface, it will dissociate into CO\* and OH\* species with a moderate barrier of 0.72 eV. Alternatively, an HCOO\* intermediate can be produced when surface H\* attacks the C atom of CO<sub>2</sub> and form a C–H bond, and this path is kinetically more conducive than COOH\* formation via an O–H bond formation, as shown in Figure 1. The activation barrier

and endothermic reaction energy for CO<sub>2</sub> hydrogenation to HCOO\* is 0.79 and 0.43 eV, respectively. Another possibility for initial conversion is direct dissociation of CO<sub>2</sub> into CO\* and O\* prior to hydrogenation, which was found to be kinetically most favorable as compared to CO<sub>2</sub> hydrogenation to the COOH\* or HCOO\* intermediate. The dissociation barrier is only 0.64 eV, and this reaction is also facile in thermodynamics, being exothermic by 1.37 eV. These calculation results on CO<sub>2</sub> initial conversion indicate that the direct dissociation to CO\* and the hydrogenation to HCOO\* are two major pathways over the  $\chi\text{-Fe}_5\text{C}_2(510)$  surface.

**3.2.2. Electronic Property Analysis on O–H Versus C–H Bond Formation.** Comparing the initial conversion of CO<sub>2</sub> hydrogenation to the COOH\* and HCOO\* intermediates, a visible difference was observed in elementary kinetics. Herein, we carried out an electronic property analysis to explain why the  $\chi\text{-Fe}_5\text{C}_2(510)$  surface exhibits such different catalytic abilities for C–H and O–H bond formation in CO<sub>2</sub> hydrogenation. The crystal orbital Hamiltonian population

(COHP) was found to be useful to analyze the bonding interaction between atoms.<sup>57,58</sup> In this work, the feasibility of C–H and O–H bonds formation in the CO<sub>2</sub> conversion path was investigated by COHP analysis. The calculated projected COHPs (pCOHPs) considering the O–H and C–H bonds interaction strength in the transition states of COOH\* and HCOO\* formation from CO<sub>2</sub> hydrogenation are shown in Figure 2. The population of the bonding region below the Fermi level (defined as integrated COHPs, iCOHPs) in TS<sub>HCOO\*</sub> ( $-1.25\text{ eV}$ ) is larger than that in TS<sub>COOH\*</sub> ( $-1.02\text{ eV}$ ), indicating that the O–H bond is weaker than the C–H bond. In addition, the COHP of the bonds between the adsorbates (HCOO and COOH) and the substrate is calculated. As shown in Figure S4, the population of the bonding region below the Fermi level (defined as integrated COHPs, iCOHPs) in the HCOO\* substrate ( $-9.91\text{ eV}$ ) is larger than that in the COOH\* substrate ( $-6.78\text{ eV}$ ), indicating a stronger interaction of the HCOO\* substrate than the COOH\* substrate. The pCOHPs and iCOHPs results demonstrate that the TS<sub>HCOO\*</sub> is more stable than TS<sub>COOH\*</sub>, and the formation of the HCOO\* intermediate would be more facile than COOH\*, in accord with the calculation results on activation barriers shown in Figure 1. Similar trends were also found in the transition states for HCO\* and COH\* formation from CO hydrogenation (see Figure 2), and the calculated iCOHPs for C–H and O–H bonds formation are  $-1.86$  and  $-1.49\text{ eV}$ , respectively, indicating that the HCO\* formation is more favorable, consistent with barrier calculations shown in Figure 3 ( $1.20\text{ eV}$  for HCO\* formation and  $1.82\text{ eV}$  for COH\* formation). The charge density diagram of the transition states related to CO<sub>2</sub> and CO hydrogenation is provided in Figure 4, from which we observed that the electron transfer properties are very different for O–H versus C–H bond formation.

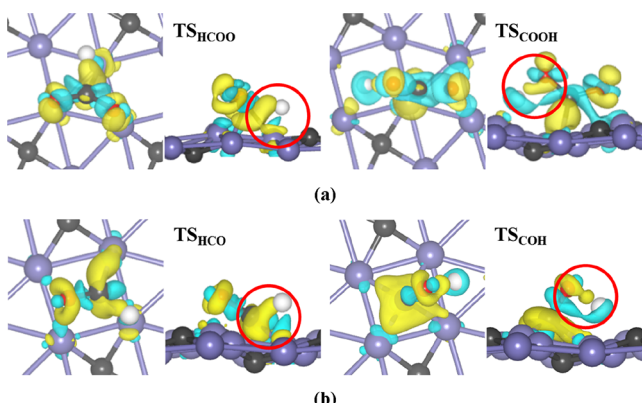


**Figure 4.** Charge density plots for C–H and O–H bonds formation in (a) CO<sub>2</sub> and (b) CO hydrogenation over  $\chi\text{-Fe}_5\text{C}_2(510)$ . Yellow and cyan isosurfaces represent the charge accumulation (i.e., a gain of electron density) and depletion (i.e., a loss of electron density), respectively.

In the formation of HCOO\* and CHO\* intermediates via C–H bond formation, the surface–adsorbate interactions are stronger. More electrons are transferred from the  $\chi\text{-Fe}_5\text{C}_2(510)$  surface to CO<sub>2</sub> or CO adsorbates, while H\* is less involved. However, for O–H bond formation, to produce COOH\* and COH\*, the surface–adsorbate interactions are not very strong. In the process of TS formation, electrons are lost when surface H\* interacts with O atoms of CO<sub>2</sub> or CO.

Moreover, the calculated Bader charge on TS<sub>HCOO</sub> and TS<sub>COOH</sub> species are  $-1.24^{\delta-}$  and  $-1.05^{\delta-}$ , respectively, indicating that the surface adsorption of TS<sub>HCOO</sub> is stronger and its transition state is more stable on the catalyst surface. A similar trend was obtained for CO hydrogenation in which the calculated Bader charge on TS<sub>CHO</sub> is more than that on TS<sub>COH</sub> ( $-1.15^{\delta-}$  vs  $-1.07^{\delta-}$ ). These calculation results on electronic properties well explained the observed distinctions in kinetic barriers between O–H and C–H bond formation in CO<sub>2</sub> and CO hydrogenation, as shown in Figures 1 and 3.

**3.2.3. CH<sub>4</sub> Production through the CO<sub>2</sub> Direct Dissociation Pathway.** In CO<sub>2</sub> hydrogenation experiments, CH<sub>4</sub> was always detected in product distribution and sometimes dominated the hydrocarbon products.<sup>3,13,14,59</sup> Based on the energy profile shown in Figure 1, CO\* was found to be a highly possible intermediate in CO<sub>2</sub> conversion over iron carbide catalyst, and herein, we first examined CH<sub>4</sub> formation through the CO<sub>2</sub> direct dissociation pathway in which the produced CO\* further dissociates into atomic C\*, and then, CH<sub>4</sub> is produced through a variety of hydrogenation steps over  $\chi\text{-Fe}_5\text{C}_2(510)$ . All intermediates and transition states of this path are shown in Figure 5, and the main structural parameters are listed in Table S3. In the transition state of CO\* and O\* dissociated from CO<sub>2</sub>, the O<sub>1</sub> atom migrates to a Fe–Fe bridge site, and the C–O<sub>1</sub> bond length is extended from  $1.34\text{ \AA}$  to  $1.77\text{ \AA}$ . The formed CO\* is adsorbed on the bridge site of Fe–Fe atoms in the final state. In the subsequent conversion of CO\*, we found that both the formation of CHO\* and COH\* via CO\* hydrogenation are energetically unfavorable due to high barriers ( $1.20$  and  $1.82\text{ eV}$ ) and strong endothermic reaction energies ( $0.84$  and  $0.91\text{ eV}$ ), consistent with the work by Pham et al. in the study of CO hydrogenation over the  $\chi\text{-Fe}_5\text{C}_2(510)$  surface.<sup>35</sup> Instead, CO\* dissociation into atomic C\* on the catalyst surface is exothermic by  $0.71\text{ eV}$ , however, the dissociation barrier is still high ( $1.44\text{ eV}$ ). In Figure 5, the atomic C\* is generated at the 4-fold hollow site, while the O atom is dissociated to a Fe–Fe bridge site in CO\* dissociation. The H\* adsorbed on the 3-fold hollow Fe site can hydrogenate the atomic C\* to form a CH\* species, which was considered to be a crucial C<sub>1</sub> intermediate in CH<sub>4</sub> and C<sub>2</sub><sup>+</sup> hydrocarbon production.<sup>37</sup> Subsequent hydrogenation of CH\* will generate CH<sub>2</sub>\* and CH<sub>3</sub>\* species and eventually produce CH<sub>4</sub>. We identified that the energetically favorable active sites for CH<sub>x</sub>\* ( $x = 0, 1, 2$ ) species adsorption are 4-fold hollow Fe sites, leading to lower barriers for C–H bond formation in hydrogenation. Our results are consistent with the previous studies by Pham et al.<sup>35</sup> and Lu et al.<sup>38</sup> The relative stabilities of CH<sub>x</sub>\* ( $x = 1–3$ ) adsorbed species relative to surface C\* are calculated according to eq 5 given below

$$E_x = E_{\text{CH}_x^*} + xE_{\text{surface}} - (E_{\text{C}^*} + xE_{\text{H}^*}) \quad (5)$$

where  $E_x$  represents the relative stability of CH<sub>x</sub>\* species relative to surface C\*,  $E_{\text{surface}}$  is the energy of the unoccupied surface,  $E_{\text{CH}_x^*}$ ,  $E_{\text{C}^*}$  and  $E_{\text{H}^*}$  are the total energy of the adsorbed CH<sub>x</sub>\*, C\*, and H\* species plus the  $\chi\text{-Fe}_5\text{C}_2(510)$  surface, respectively. The smaller the  $E_x$ , the more stable the C<sub>1</sub> species. Based on this definition, a negative  $E_x$  indicates that the CH<sub>x</sub>\* species are more stable than the adsorbed C\*. The relative stabilities of CH<sub>x</sub>\* species, given in Table S6, demonstrate that all CH<sub>x</sub>\* species are less stable than surface atomic C\* but stronger than CH<sub>2</sub>\* and CH<sub>3</sub>\* species over the  $\chi\text{-Fe}_5\text{C}_2(510)$  surface.

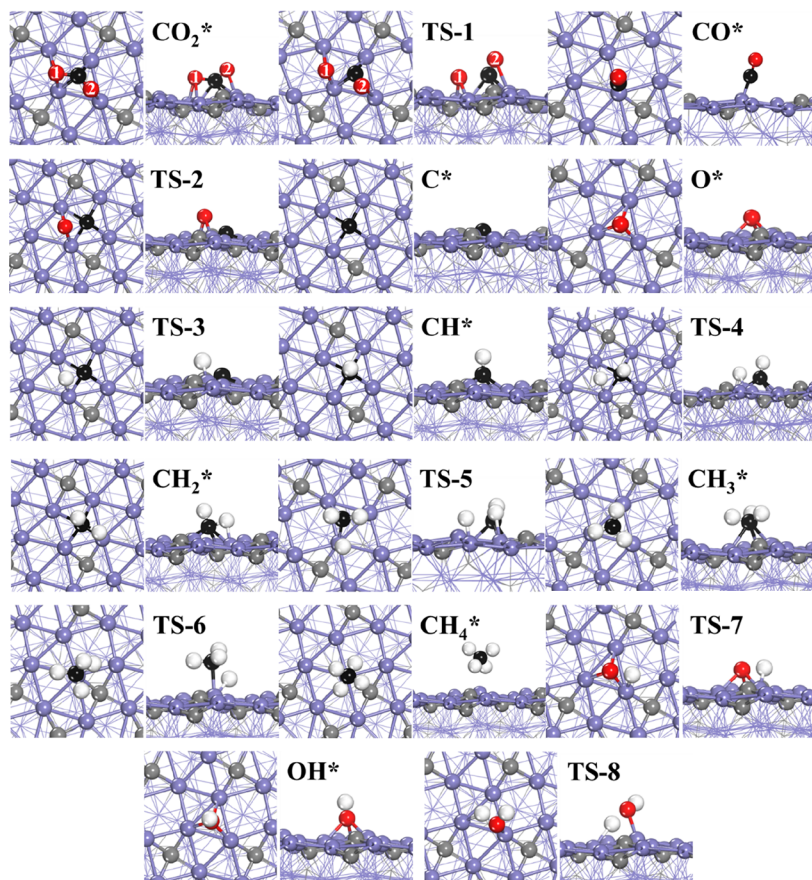


**Figure 5.** Top and side views of all states involved in  $\text{CH}_4$  production through the  $\text{CO}_2$  direct dissociation pathway over  $\chi\text{-Fe}_5\text{C}_2(510)$ . (Purple: Fe; black: C of adsorbates; red: O; white: H; and gray: C of  $\chi\text{-Fe}_5\text{C}_2$  catalyst).

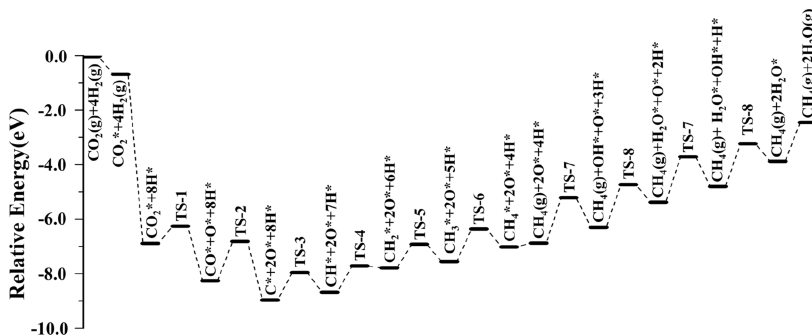


**Figure 6.** PES for  $\text{CH}_4$  production through the  $\text{CO}_2$  direct dissociation pathway over  $\chi\text{-Fe}_5\text{C}_2(510)$ .

The potential energy surface (PES) for  $\text{CH}_4$  production via the  $\text{CO}_2$  direct dissociation pathway is shown in Figure 6, from which it is observed that the rate-determining step for the formation of  $\text{CH}^*$  is the dissociation of  $\text{CO}^*$  to atomic  $\text{C}^*$ , which was calculated to be 1.44 eV. The high barrier for  $\text{CO}^*$  dissociation may be due to the fact that there is no interaction between the O atom of adsorbed  $\text{CO}^*$  and the  $\chi\text{-Fe}_5\text{C}_2(510)$  surface, and the  $\text{CO}^*$  molecule needs to be slanted toward the surface to release the O atom and break the C–O bond, which cost more energy to achieve. As for the overall reaction for  $\text{CO}_2$  conversion to methane, the effective barrier is determined by the gradual hydrogenation of atomic  $\text{C}^*$  derived from  $\text{CO}^*$  dissociation. The calculated effective barrier is 2.62 eV, which is close to the 2.81 eV reported by Pham et al.<sup>37</sup> The tough steps within this path are the dissociation of  $\text{CO}^*$  to atomic

$\text{C}^*$ , the hydrogenation of  $\text{C}^*$  to  $\text{CH}^*$ , and  $\text{CH}_3^*$  hydrogenation, making  $\text{CH}_4$  formation highly energy consuming.

**3.2.4.  $\text{CH}_4$  Production through the  $\text{HCOO}^*$  Formation Pathway.** As shown in Figure 1,  $\text{HCOO}^*$  formation is also kinetically feasible from  $\text{CO}_2$  hydrogenation, with a barrier of 0.79 eV. Herein, we examined another alternative path for  $\text{CH}_4$  production over  $\chi\text{-Fe}_5\text{C}_2(510)$  through an  $\text{HCOO}$  intermediate, as illustrated in Figure 7. The optimized structures of the transition states and intermediates within the path are illustrated in Figure 8, and crucial structural parameters are listed in Table S4. In this path, we first examined each possibility for  $\text{HCOO}^*$  conversion, including the hydrogenation to  $\text{HCOOH}^*$  and  $\text{H}_2\text{COO}^*$  or dissociation to  $\text{HCO}^* + \text{O}^*$  species on the catalyst's surface. The calculated activation barrier of  $\text{H}_2\text{COO}^*$  formation is 0.86 eV, and this

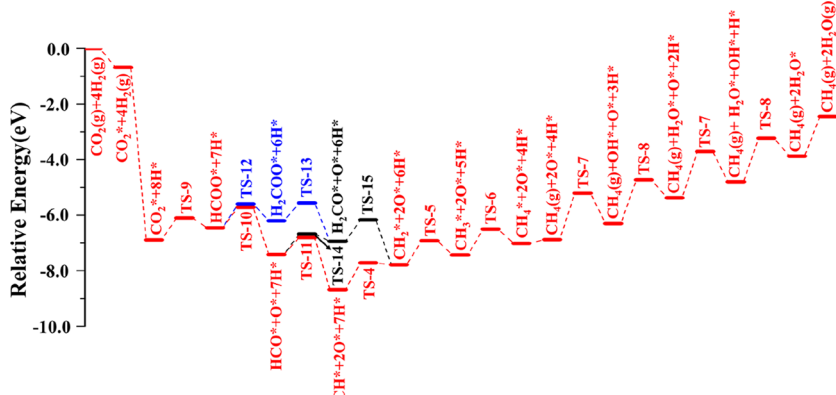


**Figure 7.** PES for  $\text{CH}_4$  production through the  $\text{HCOO}^*$  formation pathway over  $\chi\text{-Fe}_5\text{C}_2(510)$ .

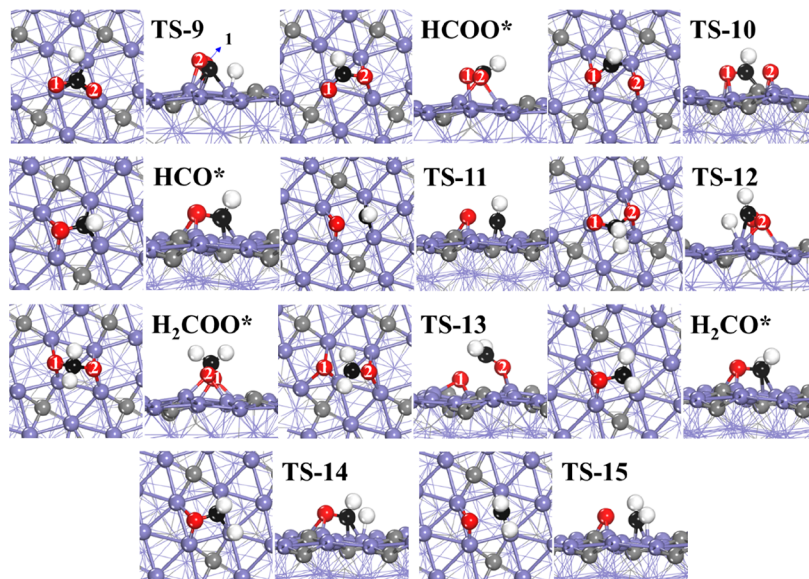


**Figure 8.** Top and side views of intermediates and transition states involved in  $\text{CH}_4$  production through the  $\text{HCOO}^*$  formation pathway over  $\chi\text{-Fe}_5\text{C}_2(510)$ . (Purple: Fe; black: C of adsorbates; red: O; white: H; and gray: C of  $\chi\text{-Fe}_5\text{C}_2$  catalyst).

reaction is slightly endothermic by 0.25 eV. The formation of  $\text{HCOOH}^*$  by  $\text{HCOO}^*$  hydrogenation does not easily occur due to a strong endothermic reaction energy (1.18 eV) and a high barrier (1.25 eV). The dissociation of  $\text{HCOO}^*$  to  $\text{HCO}^* + \text{O}^*$  is thermodynamically favorable by 0.96 eV exothermic, and the activation barrier is 0.74 eV, which is 0.12 eV lower than  $\text{H}_2\text{COO}^*$  formation via the hydrogenation of  $\text{HCOO}^*$ . These results indicate that  $\text{H}_2\text{COO}^*$  and  $\text{HCO}^* + \text{O}^*$  formations are both possible within the path.

Once  $\text{H}_2\text{COO}^*$  is produced, it can dissociate into  $\text{H}_2\text{CO}^* + \text{O}^*$  species, with a barrier of 0.64 eV (blue lines in Figure 7). Subsequent dissociation of  $\text{H}_2\text{CO}^*$  results in the formation of  $\text{CH}_2^*$  species on the catalyst's surface, with a barrier of 0.77 eV. These two dissociation steps are both exothermic, and the formation of  $\text{CH}_2^*$  is much more downhill. In the path that produces  $\text{HCO}^*$  from  $\text{HCOO}^*$  dissociation, the  $\text{HCO}^*$  can be further hydrogenated to  $\text{H}_2\text{CO}^*$  with a barrier of 0.74 eV, and this step is endothermic by 0.48 eV, indicating that the  $\text{H}_2\text{CO}^*$  intermediate is preferred to be generated via  $\text{H}_2\text{COO}^*$  dissociation rather than through  $\text{HCO}^*$  hydrogenation. Instead, the formed  $\text{HCO}^*$  intermediate will further dissociate into the  $\text{CH}^*$  species on the catalyst surface. The activation barrier for this dissociation step is 0.61 eV with the reaction

energy exothermic by 1.27 eV, showing a very facile formation of  $\text{CH}^*$  along this path. Once the  $\text{CH}^*$  species is produced,  $\text{CH}_4$  will be generated through a series of hydrogenation reactions, the same as those identified in the  $\text{CO}_2$  direct dissociation path illustrated in Figure 6. All hydrogenation reactions of  $\text{CH}_x^*$  species are uphill with kinetic barriers around 0.9–1.0 eV. The path that goes through  $\text{HCOO}^*$  hydrogenation to  $\text{H}_2\text{COO}^*$  and its dissociation to  $\text{CH}_2^*$  is energetically unfavorable as compared to the path that involves direct dissociation of  $\text{HCOO}^*$  to  $\text{HCO}^*$ , then  $\text{HCO}^*$  dissociation to  $\text{CH}^*$  and its hydrogenation to  $\text{CH}_2^*$ , as shown in Figure 7. In the latter case, the  $\text{CH}^*$  species is also a crucial  $\text{C}_1$  intermediate leading to  $\text{CH}_4$ . The highest barrier step for the formation of  $\text{CH}^*$  is  $\text{CO}_2$  hydrogenation to produce  $\text{HCO}$ , which has a barrier of 0.79 eV. For the overall reaction, the effective barrier associated with  $\text{CO}_2$  conversion to  $\text{CH}_4$  through this path was calculated to be 2.33 eV.

Comparing the two pathways for  $\text{CH}_4$  production through the  $\text{CO}_2$  direct dissociation and formation of  $\text{HCOO}^*$  intermediate, they intersect with each other at the formation of key  $\text{CH}^*$  species. The calculation results on PESs show that the effective barrier formed by  $\text{CH}^*$  in the  $\text{CO}_2$  direct dissociation pathway was 1.44 eV, which was calculated to be

1.17 eV in the  $\text{HCOO}^*$  formation pathway. Moreover, the overall reaction is also kinetically more favorable through the  $\text{HCOO}$  formation path, leading to a lower effective barrier for producing  $\text{CH}_4$  than that via the  $\text{CO}_2$  dissociation path. Therefore, the energetically preferred path to produce  $\text{CH}_4$  via  $\text{CO}_2$  hydrogenation over  $\chi\text{-Fe}_5\text{C}_2(510)$  goes through  $\text{CO}_2^* \rightarrow \text{HCOO}^* \rightarrow \text{HCO}^* \rightarrow \text{CH}^* \rightarrow \text{CH}_2^* \rightarrow \text{CH}_3^* \rightarrow \text{CH}_4^*$ .

It is worth noting that surface  $\text{O}^*$  species is always produced from dissociation reactions with the path, and its adsorption was found to be quite stable on the  $\chi\text{-Fe}_5\text{C}_2(510)$  surface, with a binding energy of  $-6.08$  eV. When the surface coverage of  $\text{O}^*$  becomes higher, it will oxidize the carbide surface to some extent, which would then impact the surface chemistry in  $\text{CO}_2$  conversion. The detailed discussions on the effect of surface  $\text{O}^*$  species on  $\text{CO}_2$  reactions will be presented in Section 3.4.2.

**3.2.5.  $\text{C}_2$  Hydrocarbons Production via  $\text{CO}_2$  Hydrogenation.** There have been theoretical studies examining  $\text{C}_2^+$  hydrocarbon production in F-T synthesis over iron carbide surfaces,<sup>37,38</sup> in which the  $\text{CH}^*$  and  $\text{CH}_2^*$  species were found to be crucial intermediates for the formation of  $\text{C}_2$  hydrocarbons on  $\chi\text{-Fe}_5\text{C}_2(510)$ . The reaction energy and activation barrier results are given in Table 1, and corresponding

**Table 1. Activation Barriers and Reaction Energies of Possible Elementary Steps Examined in  $\text{C}_2$  Hydrocarbons Formation over  $\chi\text{-Fe}_5\text{C}_2(510)$**

steps	$E_{\text{act}}$ (eV)	$\Delta E_{\text{rxn}}$ (eV)
C-C Coupling		
$2\text{CH}^* \rightarrow \text{CHCH}^*$	1.33	0.41
$\text{CH}^* + \text{CH}_2^* \rightarrow \text{CHCH}_2^*$	1.30	0.48
$2\text{CH}_2^* \rightarrow \text{CH}_2\text{CH}_2^*$	1.01	-0.15
$\text{CH}^* + \text{CH}_3^* \rightarrow \text{CHCH}_3^*$	1.74	0.72
$\text{CH}_2^* + \text{CH}_3^* \rightarrow \text{CH}_2\text{CH}_3^*$	1.09	0.08
$2\text{CH}_3^* \rightarrow \text{CH}_3\text{CH}_3(\text{g})$	2.18	0.62
$\text{C}_2$ Hydrogenation		
$\text{CHCH}^* + \text{H}^* \rightarrow \text{CHCH}_2^*$	1.20	0.97
$\text{CHCH}_2^* + \text{H}^* \rightarrow \text{CH}_2\text{CH}_2^*$	1.09	0.27
$\text{CHCH}_2^* + \text{H}^* \rightarrow \text{CHCH}_3^*$	1.14	0.47
$\text{CH}_2\text{CH}_2^* + \text{H}^* \rightarrow \text{CH}_2\text{CH}_3^*$	1.16	0.58
$\text{CHCH}_3^* + \text{H}^* \rightarrow \text{CH}_2\text{CH}_3^*$	0.92	0.38
$\text{CH}_2\text{CH}_3^* + \text{H}^* \rightarrow \text{CH}_3\text{CH}_3(\text{g})$	1.32	0.64

structures of the transition state and intermediate for each elementary step are provided in Figure S5. In previous DFT work,<sup>37,60</sup> the C–C couplings of surface  $\text{C}^*$  with other  $\text{CH}_x^*$  species were found to be difficult, and thus, these reactions were excluded in this work. The most stable site for  $\text{CH}_x^*$

adsorption is the 4-fold hollow site, and the formation of  $\text{C}_2$  species needs an adjacent 3-fold hollow site to achieve C–C coupling.

We identified that the  $\text{CH}^*$  species is the energetically most favorable  $\text{C}_1$  intermediate for higher hydrocarbon production and the coupling of two  $\text{CH}^*$  species over  $\chi\text{-Fe}_5\text{C}_2(510)$  may lead to the formation of the first C–C bond. The kinetic barrier for this reaction was calculated to be 1.33 eV, higher than those for sequential  $\text{CH}^*$  hydrogenation to produce  $\text{CH}_4$ . The coupling of  $\text{CH}^*$  with  $\text{CH}_2^*$  also requires overcoming a barrier of 1.30 eV. Based on the results given in Table 1, the energetically favorable C–C couplings are  $\text{CH}_2^*$  with  $\text{CH}_2^*$  and  $\text{CH}_2^*$  with  $\text{CH}_3^*$ . Due to a high barrier of 2.18 eV, direct coupling between two  $\text{CH}_3^*$  species is dynamically impossible. For  $\text{C}_2$  species hydrogenation reactions, all barriers are higher than 0.9 eV, especially for  $\text{C}_2\text{H}_6$  formation through  $\text{CH}_2\text{CH}_3^*$  hydrogenation, which has a barrier of 1.32 eV. The energetically favorable path for  $\text{C}_2\text{H}_4$  formation is through direct coupling of two  $\text{CH}_2^*$  intermediates, and further conversion of  $\text{C}_2\text{H}_4$  to  $\text{C}_2\text{H}_6$  would be slow on the catalyst surface because the hydrogenation barriers are not small. These C–C coupling and hydrogenation steps are almost uphill with substantial barriers, indicating that the production of  $\text{C}_2$  hydrocarbons is slow over the  $\chi\text{-Fe}_5\text{C}_2(510)$  surface.

**3.2.6. Impact of C-vacancy on  $\text{CO}_2$  Conversion.** In literature, there have been studies exploring the effect of C-vacancy formation during F-T synthesis on the iron carbide catalysts.<sup>37,39</sup> The presence of C-vacancy over the iron carbide surface would impact the adsorption stability of reactants and intermediates, thus altering reaction pathways for  $\text{CO}_2$  reactions. In this work, we investigated the formation mechanism of C vacancy over  $\chi\text{-Fe}_5\text{C}_2(510)$  and its effect on  $\text{CO}_2$  adsorption and conversion. The optimized structures of all states involved in these reactions are shown in Figure S6. Through a series of hydrogenation steps of the surface C atom of  $\chi\text{-Fe}_5\text{C}_2(510)$  and desorption of the formed  $\text{CH}_4$  species, a C-vacancy can be generated on the catalyst's surface. However, these hydrogenation steps are all uphill, with the overall reaction energy being endothermic by 2.04 eV and an effective barrier of 2.81 eV, as shown in the energy diagram plotted in Figure 9. The adsorption energy of  $\text{CO}_2$  molecules on the C-vacancy of the catalyst surface is  $-1.04$  eV, which is 0.36 eV higher than that on the perfect surface. Then, the adsorbed  $\text{CO}_2$  prefers to dissociate into  $\text{CO}^*$  rather than hydrogenate to  $\text{HCOO}^*$  due to the favorability in both the reaction energy and activation barrier (see Figure 9) for dissociation. The produced  $\text{CO}^*$  will further dissociate into atomic  $\text{C}^*$  adsorbed

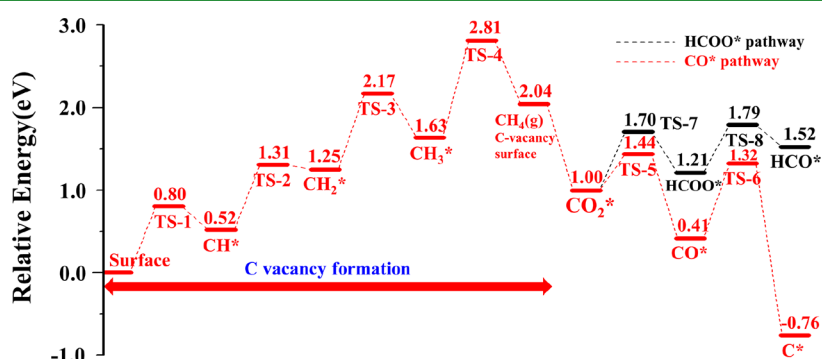


**Figure 9.** Mechanism and energy profile for C vacancy formation as well as  $\text{CO}_2$  conversion on the defect  $\chi\text{-Fe}_5\text{C}_2(510)$  surface.

**Table 2.** Activation Barriers, Reaction Energies, and Forward/Reverse Pre-exponential Factors of All Elementary Steps Examined in the Pathways of CO<sub>2</sub> Conversion on  $\chi$ -Fe<sub>5</sub>C<sub>2</sub>(S10)

entry	elementary steps	$\Delta E$	$\Delta E^{\text{ZPC}}$	$\Delta G$	$E_a$	$E_a^{\text{ZPC}}$	$A_{\text{Fwd}}$	$A_{\text{Rev}}$
1	CO <sub>2</sub> (g) + * → CO <sub>2</sub> *	-0.68	-0.70	0.44	0.00	0.00	$4.35 \times 10^7$	$1.44 \times 10^{16}$
2	H <sub>2</sub> (g) + 2* → 2H*	-1.55	-1.45	-0.63	0.00	0.00	$2.04 \times 10^8$	$3.08 \times 10^{14}$
3	CO <sub>2</sub> * + H* → HCOO* + *	0.43	0.55	0.44	0.79	0.77	$1.21 \times 10^{13}$	$1.97 \times 10^{12}$
4	HCOO* + * → HCO* + O*	-0.96	-1.01	-0.87	0.74	0.70	$1.24 \times 10^{12}$	$1.43 \times 10^{13}$
5	HCOO* + H* → H <sub>2</sub> COO* + *	0.25	0.42	0.53	0.86	0.91	$1.04 \times 10^{12}$	$7.70 \times 10^{12}$
6	H <sub>2</sub> COO* + * → H <sub>2</sub> CO* + O*	-0.74	-0.85	-0.83	0.64	0.55	$3.64 \times 10^{13}$	$4.75 \times 10^{13}$
7	HCO* + * → CH* + O*	-1.27	-1.30	-1.29	0.61	0.56	$9.53 \times 10^{12}$	$1.21 \times 10^{13}$
8	HCO* + H* → H <sub>2</sub> CO* + *	0.48	0.58	0.56	0.74	0.73	$1.17 \times 10^{13}$	$9.24 \times 10^{12}$
9	H <sub>2</sub> CO* + * → CH <sub>2</sub> * + O*	-0.84	-0.96	-0.97	0.77	0.69	$8.65 \times 10^{12}$	$7.15 \times 10^{12}$
10	CH* + H* → CH <sub>2</sub> * + *	0.90	0.92	0.88	0.97	0.94	$1.24 \times 10^{13}$	$6.17 \times 10^{12}$
11	CH <sub>2</sub> * + H* → CH <sub>3</sub> * + *	0.35	0.52	0.43	0.87	0.88	$1.81 \times 10^{13}$	$4.17 \times 10^{12}$
12	CH <sub>3</sub> * + H* → CH <sub>4</sub> * + *	0.42	0.54	0.35	1.08	1.05	$1.54 \times 10^{13}$	$6.27 \times 10^{11}$
13	2CH* → C <sub>2</sub> H <sub>2</sub> * + *	0.41	0.47	0.46	1.33	1.34	$8.71 \times 10^{12}$	$7.72 \times 10^{12}$
14	CH* + CH <sub>2</sub> * → C <sub>2</sub> H <sub>3</sub> * + *	0.48	0.59	0.59	1.30	1.35	$5.92 \times 10^{12}$	$6.22 \times 10^{12}$
15	C <sub>2</sub> H <sub>2</sub> * + H* → C <sub>2</sub> H <sub>3</sub> * + *	0.97	1.04	1.01	1.20	1.17	$2.23 \times 10^{13}$	$1.32 \times 10^{13}$
16	C <sub>2</sub> H <sub>3</sub> * + H* → C <sub>2</sub> H <sub>4</sub> * + *	0.27	0.44	0.38	1.09	1.07	$1.34 \times 10^{13}$	$4.93 \times 10^{12}$
17	2CH <sub>2</sub> * → C <sub>2</sub> H <sub>4</sub> * + *	-0.15	0.11	0.09	1.01	1.16	$7.96 \times 10^{12}$	$6.19 \times 10^{12}$
18	CH <sub>2</sub> * + CH <sub>3</sub> * → C <sub>2</sub> H <sub>3</sub> * + *	0.08	0.26	0.29	1.09	1.17	$1.57 \times 10^{13}$	$2.60 \times 10^{13}$
19	C <sub>2</sub> H <sub>4</sub> * + H* → C <sub>2</sub> H <sub>5</sub> * + *	0.58	0.67	0.63	1.16	1.11	$1.04 \times 10^{13}$	$5.05 \times 10^{12}$
20	C <sub>2</sub> H <sub>5</sub> * + H* → C <sub>2</sub> H <sub>6</sub> (g) + 2*	0.64	0.78	-0.35	1.32	1.31	$2.47 \times 10^{13}$	$7.88 \times 10^4$
21	CO <sub>2</sub> * + * → CO* + O*	-1.37	-1.38	-1.47	0.64	0.58	$2.47 \times 10^{13}$	$5.51 \times 10^{12}$
22	CO* + * → C* + O*	-0.71	-0.74	-0.59	1.44	1.38	$7.36 \times 10^{11}$	$9.99 \times 10^{12}$
23	CO* + H* → HCO* + *	0.84	0.92	1.04	1.20	1.16	$1.58 \times 10^{12}$	$1.34 \times 10^{13}$
24	CO* + H* → COH* + *	0.91	0.99	1.02	1.82	1.70	$4.53 \times 10^{12}$	$8.06 \times 10^{12}$
25	COH* + * → C* + OH*	-1.05	-1.06	-1.00	1.11	1.06	$3.43 \times 10^{12}$	$9.90 \times 10^{12}$
26	C* + H* → CH* + *	0.29	0.36	0.35	1.02	0.96	$1.49 \times 10^{13}$	$1.18 \times 10^{13}$
27	CO <sub>2</sub> * + H* → COOH* + *	0.34	0.48	0.41	1.23	1.15	$3.48 \times 10^{13}$	$1.03 \times 10^{13}$
28	COOH* + * → CO* + OH*	-1.13	-1.18	-1.25	0.72	0.64	$9.36 \times 10^{12}$	$2.69 \times 10^{12}$
29	O* + H* → OH* + *	0.58	0.68	0.62	1.67	1.60	$2.65 \times 10^{13}$	$1.00 \times 10^{13}$
30	OH* + H* → H <sub>2</sub> O* + *	0.92	1.03	0.85	1.57	1.47	$5.41 \times 10^{13}$	$2.48 \times 10^{12}$
31	H <sub>2</sub> O* → * + H <sub>2</sub> O(g)	0.71	0.64	-0.26	0.71	0.64	$3.58 \times 10^{14}$	$6.81 \times 10^7$
32	CO* → * + CO(g)	2.12	2.04	1.03	2.12	2.04	$2.34 \times 10^{15}$	$5.46 \times 10^7$
33	C <sub>2</sub> H <sub>4</sub> * → * + C <sub>2</sub> H <sub>4</sub> (g)	1.43	1.41	0.25	1.43	1.41	$2.33 \times 10^{16}$	$5.46 \times 10^7$
34	CH <sub>4</sub> * → * + CH <sub>4</sub> (g)	0.14	0.11	-0.87	0.14	0.11	$5.02 \times 10^{14}$	$6.97 \times 10^7$

at the vacancy site to regenerate the perfect  $\chi$ -Fe<sub>5</sub>C<sub>2</sub>(S10) surface, with a barrier of 0.91 eV. The CO<sub>2</sub> hydrogenation to HCOO\* over the defect  $\chi$ -Fe<sub>5</sub>C<sub>2</sub>(S10) surface requires overcoming the 0.70 eV barrier, close to that obtained on the perfect surface. The subsequent HCOO\* dissociation into HCO\* and O\* has a barrier of 0.58 eV, 0.16 eV lower than that calculated on the perfect surface. These results suggest that the defect  $\chi$ -Fe<sub>5</sub>C<sub>2</sub>(S10) surface favors the cleavage of the C–O bond, while has a slight effect on C–H bond formation. Although the presence of C-vacancy can enhance CO<sub>2</sub> adsorption and may impact the pathways for CO<sub>2</sub> conversion, the calculation results already demonstrated that the formation of C-vacancy on  $\chi$ -Fe<sub>5</sub>C<sub>2</sub>(S10) requires overcoming high barriers and that the overall reaction is endothermic by 2.04 eV. Therefore, we carried on the following studies based on the perfect  $\chi$ -Fe<sub>5</sub>C<sub>2</sub>(S10) surface without C-vacancy.

The above mentioned calculation results on elementary steps and PESs provide mechanistic insight into the preferred pathways for CO<sub>2</sub> hydrogenation to C<sub>1</sub> (CO and CH<sub>4</sub>) as well as C<sub>2</sub> (C<sub>2</sub>H<sub>4</sub>, and C<sub>2</sub>H<sub>6</sub>) hydrocarbons over  $\chi$ -Fe<sub>5</sub>C<sub>2</sub>(S10). However, if one wants to assess the rates and relative selectivities of these products, the microkinetic modeling study is indispensable to combine with DFT, which will be discussed in detail in Section 3.3 below.

**3.3. Microkinetic Modeling Study on CO<sub>2</sub> Hydrogenation.** A microkinetic modeling study applying the mean-field and steady-state approximation was performed to investigate the surface coverage of key intermediates and evaluate the relative selectivities of key products. Table 2 lists the key parameters used for microkinetic modeling including activation barriers, reaction energies, and forward/reverse pre-exponential factors of elementary steps considered in this work. The ZPE correction is considered, and detailed ZPE values are given in Table 2. The corresponding temperature and pressure are 623 K and 30 bar, respectively, which is consistent with the experimental conditions.<sup>22</sup>

Figure 10 shows the surface coverages of key species of H\*, O\*, CO\*, and CH\* at different temperatures, from which we found that these species almost occupied the catalyst surface with a very small fraction of free sites. The surface coverages of O\* and CO\* decrease, while the surface coverages of H\* and CH\* increase as the temperature goes up. Among them, with the increase in temperature, both CO<sub>2</sub> and H<sub>2</sub> on the surface of Fe<sub>5</sub>C<sub>2</sub> are easily dissociated, and H<sub>2</sub> is more easily dissociated than CO<sub>2</sub>. As a result, the surface coverage of H\* increases gradually, while that of CO\* and O\* decreases gradually compared with that of H\*. In addition, the CO\* intermediates desorb with increasing temperature, so the surface coverage of

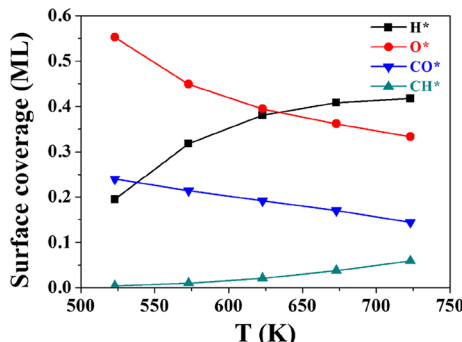


**Figure 10.** Surface coverages of key species under different temperatures over  $\chi\text{-Fe}_5\text{C}_2(510)$ .

$\text{CO}^*$  decreases. The increased surface coverage of  $\text{H}^*$  can promote the continuous hydrogenation of surface intermediates, thus improving the surface coverage of key  $\text{CH}^*$  species. In detail, when the temperature is lower than 623 K, the surface coverage of  $\text{O}^*$  species is the highest which will lead to partial oxidation of the iron carbide surface. The high concentration of  $\text{O}^*$  species on the surface impedes the C–C couplings as we did observe lower surface coverage of  $\text{CH}^*$  species within the temperature range examined, as shown in Figure 10. In addition, when the temperature is lower than 623 K, the surface coverage of  $\text{O}^*$  species is highest, which will easily lead to partial oxidation of the iron carbide surface. The high concentration of  $\text{O}^*$  species on the surface impedes C–C couplings as we did observe lower surface coverage of  $\text{CH}^*$  species within the temperature range examined, as shown in Figure 10. Our experimental studies performed at 593 and 673 K showed that certain amount of  $\text{Fe}_3\text{O}_4$  species was produced after  $\text{CO}_2$  hydrogenation reaction over  $\text{Fe}_5\text{C}_2$  catalysts, indicating that the oxidation of the carbide surface occurred during reaction, agreeing with the computational results that shows high surface  $\text{O}^*$  coverage under experimental conditions.<sup>61</sup>

To determine the relative selectivities of  $\text{CO}_2$  conversion products over  $\chi\text{-Fe}_5\text{C}_2(510)$ , we plotted the dependence of TOFs of  $\text{CH}_4$ ,  $\text{CO}$ ,  $\text{C}_2\text{H}_4$ , and  $\text{C}_2\text{H}_6$  on the reaction temperature, as illustrated in Figure 11. It was found that the TOFs of these products are enhanced with increasing temperature. The selectivity of  $\text{CH}_4$  is the highest among these products, followed by  $\text{CO}$ ,  $\text{C}_2\text{H}_4$ , and  $\text{C}_2\text{H}_6$ . The relative selectivity of  $\text{C}_2$  hydrocarbons is lower than that of  $\text{CH}_4$ , which may be attributed to the high coverage of surface  $\text{O}^*$  that can

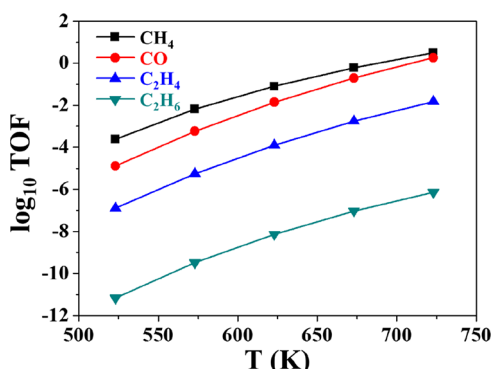


**Figure 11.** TOFs of major products from  $\text{CO}_2$  hydrogenation under different temperatures over  $\chi\text{-Fe}_5\text{C}_2(510)$ .

occupy the crucial 3-fold hollow sites for C–C couplings and carbon chain growth.

In the experimental work carried out by Bordet et al.,<sup>62</sup> they investigated  $\text{CO}_2$  hydrogenation over iron carbide catalysts and found that the selectivity of  $\text{CH}_4$  is higher than that of  $\text{C}_2$  hydrocarbons, consistent with our results. However, they identified that the selectivity of  $\text{CO}$  is almost equal to that of  $\text{C}_2$  hydrocarbons, which is not observed in our calculation (see Figure 11). This disagreement may have resulted from the exclusion of the surface coverage effect and competitive adsorption on the adsorption energies of key surface species, which will be taken into account in our future work.

**3.4. Discussion.** **3.4.1. Comparison of  $\text{CO}_2$  and  $\text{CO}$  Hydrogenation for Hydrocarbon Synthesis.** In this section, we performed a microkinetic modeling study to compare the hydrogenation properties between  $\text{CO}_2$  and  $\text{CO}$  as reactants. The results are given in Table 3. The TOFs of both  $\text{CH}_4$  and

**Table 3. Surface Coverages of Key Intermediates and TOFs of  $\text{CH}_4$  and  $\text{C}_2\text{H}_4$  in  $\text{CO}_2$  and  $\text{CO}$  Hydrogenation at 623 K over  $\chi\text{-Fe}_5\text{C}_2(510)$**

items	surface coverage	
	$\text{CO}_2$	$\text{CO}$
$\text{H}^*$	$3.80 \times 10^{-1}$	$1.39 \times 10^{-4}$
$\text{O}^*$	$3.95 \times 10^{-1}$	$3.25 \times 10^{-1}$
$\text{CO}^*$	$1.92 \times 10^{-1}$	$4.60 \times 10^{-1}$
$\text{CH}^*$	$2.09 \times 10^{-2}$	$3.36 \times 10^{-2}$
TOF of $\text{C}_2\text{H}_4$ ( $\text{s}^{-1}$ )	$1.27 \times 10^{-4}$	$2.41 \times 10^{-6}$
TOF of $\text{CH}_4$ ( $\text{s}^{-1}$ )	$7.86 \times 10^{-2}$	$1.90 \times 10^{-6}$
T (K)	623	623
$P_{\text{CO}_2}$ or $P_{\text{CO}}$ (bar)	7.5	10
$P_{\text{H}_2}$ (bar)	22.5	20

$\text{C}_2\text{H}_4$  are higher from  $\text{CO}_2$  hydrogenation than via  $\text{CO}$  hydrogenation, indicating that  $\text{CO}_2$  hydrogenation would proceed faster than that of  $\text{CO}$  under similar conditions. The crucial intermediate for  $\text{CH}_4$  and  $\text{C}_2\text{H}_4$  production is  $\text{CH}^*$ , which is produced by the dissociation of  $\text{HCO}^*$  in  $\text{CO}_2$  hydrogenation and the hydrogenation of  $\text{C}^*$  in  $\text{CO}$  hydrogenation, respectively. The notable difference between  $\text{CO}_2$  and  $\text{CO}$  hydrogenation is the effective barrier for  $\text{CH}^*$  formation (1.17 eV in  $\text{CO}_2$  hydrogenation vs 1.44 eV in  $\text{CO}$  hydrogenation), showing an advantage when  $\text{CO}_2$  was used as the reactant. Moreover, the effective barrier of  $\text{CH}_4$  formation from  $\text{CO}_2$  hydrogenation is 2.33 eV, which is also lower than that from  $\text{CO}$  hydrogenation (2.62 eV).

For product selectivity,  $\text{CH}_4$  dominates the product distribution in  $\text{CO}_2$  hydrogenation, whereas the relative selectivity of  $\text{C}_2\text{H}_4$  is higher than  $\text{CH}_4$  in  $\text{CO}$  hydrogenation, showing very different reaction properties between  $\text{CO}_2$  and  $\text{CO}$  conversions over the  $\chi\text{-Fe}_5\text{C}_2(510)$  surface. Our prediction of the selectivity trend from  $\text{CO}$  hydrogenation is consistent with the previous experimental work by Yang et al.<sup>31</sup> A major difference between  $\text{CO}_2$  and  $\text{CO}$  hydrogenation conditions comes from the surface coverage of major species (such as  $\text{H}^*$  and  $\text{CH}_x^*$ ), which can impact the C–C coupling and hydrogenation activity, thus alter the relative selectivity to  $\text{CH}_4$  and  $\text{C}_2$  hydrocarbons. In regard to  $\text{CO}$  hydrogenation, the  $\text{CO}^*$  species prefers to be adsorbed at the top  $\chi\text{-Fe}_5\text{C}_2(510)$  sites and thereof providing more 3-fold hollow sites for  $\text{CH}_x$  species adsorption to achieve C–C coupling,

leading to a higher selectivity for  $C_2$  hydrocarbons from CO hydrogenation. While for  $CO_2$  hydrogenation, the high surface coverage of  $O^*$  and  $H^*$  species adsorbed on 3-fold hollow sites would impede C–C couplings between  $CH_x$  species and against chain growth possibility. Consequently, a higher  $CH_4$  selectivity was obtained in  $CO_2$  hydrogenation but higher  $C_2H_4$  selectivity was achieved under CO hydrogenation conditions.

**3.4.2. Impact of Surface  $O^*$  Coverage on  $C_2$  Hydrocarbons Formation.** Within the pathways in  $CO_2$  hydrogenation to hydrocarbons, we found stable  $O^*$  species adsorbed on the catalyst surface, and the binding energy was  $-6.08\text{ eV}$ . We then calculated the barriers for hydrogenation of surface  $O^*$  to  $OH^*$  species and then for the formation of  $H_2O^*$  over  $\chi\text{-Fe}_5C_2(510)$ . The  $O^*$  hydrogenation to  $OH^*$  requires overcoming a barrier of  $1.67\text{ eV}$ , and the formation of  $H_2O^*$  through  $OH^*$  hydrogenation has a barrier of  $1.57\text{ eV}$ , as observed in Figure 6. The strong adsorption energy of  $O^*$  and high hydrogenation barriers for  $O^*$  conversion to  $H_2O^*$  result in high coverage of  $O^*$  on the carbide surface, which will oxidize the carbide surface to some extent and impact the formation of  $C_2^+$  hydrocarbons. For a further understanding of the role of surfaces  $O^*$  species on the rates for  $CH_4$  and  $C_2H_4$  formation, the degree of rate control (DRC) analysis<sup>63,64</sup> was carried out to identify the kinetic controlling steps in  $CH_4$  and  $C_2H_4$  production pathways from  $CO_2$  hydrogenation. The  $O^* + H^* \rightarrow OH^*$  and  $OH^* + H^* \rightarrow H_2O^*$  steps have relatively larger DRC values (e.g.,  $\sim 0.7$  and  $\sim 0.5$ , respectively, for  $CH_4$  and  $C_2H_4$  formation at  $523\text{ K}$ ), which can significantly impact the rates for  $CH_4$  and  $C_2H_4$  production. Figure 12 shows the

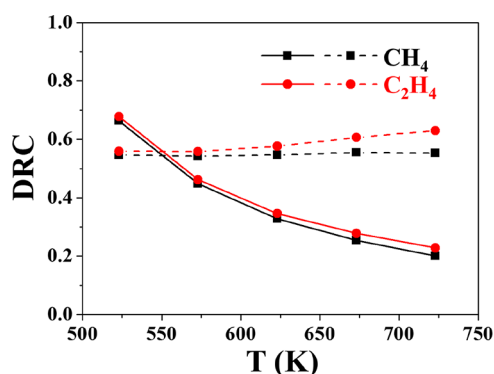


**Figure 12.** DRCs of surface  $O^*$  and  $OH^*$  hydrogenation for  $CH_4$  and  $C_2H_4$  production under  $CO_2$  hydrogenation conditions. (Solid line:  $O^* + H^* \rightarrow OH^*$ ; dashed line:  $OH^* + H^* \rightarrow H_2O^*$ ).

DRC values of surface  $O^*$  and  $OH^*$  hydrogenation reactions for  $CH_4$  and  $C_2H_4$  production under  $CO_2$  hydrogenation conditions. At temperatures below  $550\text{ K}$ , both the hydrogenation of surface  $O^*$  and subsequent hydrogenation of  $OH^*$

have a substantial impact on  $CH_4$  and  $C_2H_4$  formation rates. With the increase in temperature, the effect of  $O^*$  hydrogenation to  $OH^*$  is reduced, while the impact of the formed  $OH^*$  species hydrogenation to  $H_2O^*$  on the TOFs of  $CH_4$  and  $C_2H_4$  formation is still overwhelming (DRCs above 0.5), especially for  $C_2H_4$  formation at a higher temperature. Overall, the negative effect of conversion of surface  $O^*$  species to  $H_2O^*$  on  $C_2H_4$  formation is larger than that for  $CH_4$ , which could, to a certain extent, explain the observed higher  $CH_4$  selectivity than  $C_2H_4$  obtained from  $CO_2$  hydrogenation over the  $\chi\text{-Fe}_5C_2(510)$  surface.

Based on the calculation results from DFT and microkinetic modeling, it was found that a crucial issue on  $C_2$  hydrocarbon synthesis via  $CO_2$  hydrogenation over  $\chi\text{-Fe}_5C_2$  catalyst is the formation of stable  $O^*$  species, which can partially oxidize the iron carbide surface. In the previous experimental results,  $Fe_3O_4$  and  $Fe_5C_2$  are found to be the main phases of spent catalysts.<sup>23,65</sup> Both iron carbide and oxide play a role in higher hydrocarbon synthesis. Therefore, the performance of  $CO_2$  hydrogenation may be correlated with the interfacial sites between iron carbide and oxide. A coexisted phase containing iron oxide and carbide would be produced under  $CO_2$  conversion conditions, which may act as bi-functional active sites for hydrocarbons formation.<sup>65</sup> Another possibility is the creation of interfacial sites between iron oxide and carbide phases, which can impact the adsorption stability of surface species, reaction pathways, and selectivity. We constructed a mixed surface model containing interfacial sites between iron oxide and carbide, as depicted in Figure 13, based on which the  $O^*$  species hydrogenation to  $OH^*$  and then to  $H_2O^*$  at the interfacial site was examined. The optimized structures of all states included in the above mentioned reactions are shown in Figure S7. The calculated activation barriers of  $OH^*$  and  $H_2O^*$  formation steps decreased to  $0.74$  and  $0.91\text{ eV}$ , respectively, showing apparent favorability of interfacial sites in the promotion of O–H bond formation. Meanwhile, the removal of surface  $O^*$  species can minimize the oxidation of the carbide phase and release more crucial active sites for  $CH_x$  species adsorption and C–C bond formation, thus enhancing the selectivity of  $C_2^+$  hydrocarbons. Calculations on the whole path for hydrocarbon production via  $CO_2$  hydrogenation over the mixed surface model of iron oxide and carbide-containing interfacial sites will be introduced in our future work.

**3.4.3. Impact of Adding K on the Conversion of Surface  $O^*$  Species.** Alkali metals, such as K, have been widely used as promoters of  $CO_2$  hydrogenation over iron-based catalysts. K-modified  $Fe_5C_2$  can advance the selectivity to higher hydrocarbons under  $CO_2$  hydrogenation conditions.<sup>67</sup> Experimentally, the presence of K can improve the selectivity of higher hydrocarbons and enhance the yield of olefin-rich hydrocarbons.<sup>12,15,16,66</sup> Here, we examined the effect of potassium on the surface  $O^*$  species removal over  $\chi\text{-Fe}_5C_2$ .

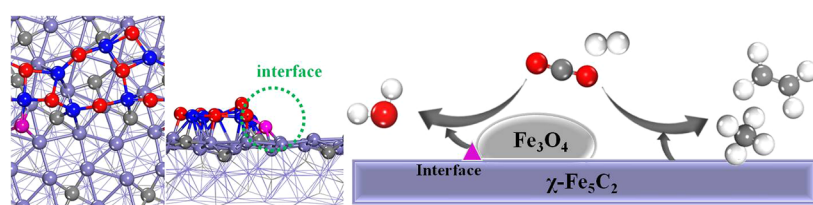


**Figure 13.** Mixed surface model of iron oxide and  $\chi\text{-Fe}_5C_2$  containing interfacial sites. (Purple: Fe of  $\chi\text{-Fe}_5C_2$ ; gray: C; blue: Fe of iron oxide; red: O; and purple: surface  $O^*$ ).

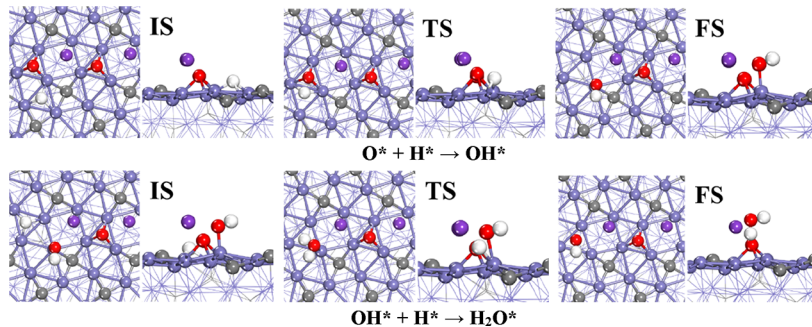


**Figure 14.** Initial, transition, and final states associated with  $\text{OH}^*$  and  $\text{H}_2\text{O}^*$  formation on the  $\text{K}_2\text{O}$ -adsorbed  $\chi\text{-Fe}_5\text{C}_2(510)$  surface.

$\text{Fe}_5\text{C}_2(510)$ , and the involved optimized structures are shown in Figure 14. In the presence of  $\text{K}_2\text{O}$ , the barriers for hydrogenation of  $\text{O}^*$  and  $\text{OH}^*$  are observably reduced to 0.30 and 0.79 eV, respectively. The great advantages of using potassium promoter are to remove surface  $\text{O}^*$  species fast, minimize the oxidation of carbide catalyst, enhance the stability of iron carbide phase, and promote C–C couplings and carbon chain growth. This result agrees with the previous experimental study by Niu et al.<sup>67</sup> regarding the potassium promotion on tuning carburization behaviors of iron catalysts and the computational studies by Wang et al.<sup>68–70</sup> on the promotion of  $\text{O}^*$  and  $\text{OH}^*$  hydrogenation to water by potassium addition, which proposed that the presence of potassium facilitates  $\text{O}^*$  removal and the carburization of iron catalysts.

Bordet et al.<sup>62</sup> investigated the impact of water removal on catalyst phase transformation and  $\text{CO}_2$  hydrogenation properties over iron carbide catalyst. They found that the removal of  $\text{H}_2\text{O}$  formed by the hydrogenation of  $\text{O}^*$  could facilitate the carbonization of iron nanoparticles and increase the selectivity of hydrocarbons such as  $\text{C}_3$  products. Their results confirm our deduction that surface  $\text{O}^*$  species has an important impact on the relative selectivities of  $\text{CH}_4$  and higher hydrocarbons. Based on the results of this work, one option in the design strategy of highly selective  $\text{CO}_2$  hydrogenation catalysts for hydrocarbon synthesis is introducing appropriate promoters such as potassium to stabilize the iron carbide phase and tune the adsorption properties and competitive adsorptions of key surface species, such as  $\text{H}^*$ ,  $\text{O}^*$ , and  $\text{CH}_x^*$ , which would then impact the pathways, kinetics, and selectivity. Furthermore, combining the iron oxide and iron carbide catalysts to create more interfacial sites can speed up surface  $\text{O}^*$  removal which also has a potential impact on  $\text{CO}_2$  conversion chemistry. Another potential approach is adding second active components into Fe-based catalysts such as Pt, Cu, and Au, which exhibit good activity for  $\text{H}_2\text{O}$  formation in RWGS reactions, to reduce the binding energy of  $\text{O}^*$  and facilitate surface  $\text{O}^*$  removal via hydrogenation.

## 4. CONCLUSIONS

In summary, the energetically favorable pathways for hydrocarbon synthesis from  $\text{CO}_2$  hydrogenation over the  $\chi\text{-Fe}_5\text{C}_2(510)$  surface are identified using DFT calculations, which go through an  $\text{HCOO}^*$  intermediate and a key  $\text{CH}^*$  intermediate that lead to  $\text{CH}_4$  and  $\text{C}_2\text{H}_4$  formation. Microkinetic modeling is used to identify kinetic controlling steps for  $\text{CO}_2$  conversion and evaluate the relative selectivities of key products including  $\text{CO}$ ,  $\text{CH}_4$ ,  $\text{C}_2\text{H}_4$ , and  $\text{C}_2\text{H}_6$ . It is found that the selectivity to  $\text{CH}_4$  is higher than  $\text{C}_2\text{H}_4$  in  $\text{CO}_2$

hydrogenation but is lower under CO hydrogenation conditions. The major distinction between  $\text{CO}_2$  and CO hydrogenation lies in the different surface coverages of key species such as  $\text{H}^*$ ,  $\text{CH}_x^*$  and  $\text{O}^*$ , which can impact the C–C coupling versus hydrogenation activity over  $\chi\text{-Fe}_5\text{C}_2(510)$ . The high surface coverage of  $\text{O}^*$  in  $\text{CO}_2$  hydrogenation can oxidize the carbide surface and result in the coexistence of iron oxide and carbide phases under reaction conditions. The interfacial sites between  $\text{Fe}_5\text{C}_2\text{-Fe}_2\text{O}_3$  created on the mixed surfaces facilitate the conversion of adsorbed  $\text{O}^*$  to  $\text{H}_2\text{O}^*$  to release more active sites for adsorptions of  $\text{CH}_x$  species and C–C couplings to produce hydrocarbons. Furthermore, adding a potassium promoter to the  $\text{Fe}_5\text{C}_2$  catalyst can accelerate  $\text{O}^*$  removal from the carbide surface, enhance the stability of the iron carbide catalyst, and promote C–C couplings for hydrocarbon synthesis. The computational models simulate the morphology of catalysts under the conditions of infinitely close to real reactions. Our calculation results show that the design of the interface between iron carbide and iron oxide will be of great benefit to improve the oxidation resistance of the catalyst, thus, improving the stability of the catalyst and facilitating the synthesis of higher hydrocarbons, providing useful guidance for future catalyst design.

## ASSOCIATED CONTENT

### Supporting Information

The Supporting Information is available free of charge at <https://pubs.acs.org/doi/10.1021/acsami.2c07029>.

Configurations and corresponding energy data of initial, transition, and final states involved in  $\text{CO}_2$  hydrogenation on  $\chi\text{-Fe}_5\text{C}_2(510)$  ([PDF](#))

## AUTHOR INFORMATION

### Corresponding Authors

Xiaowa Nie – State Key Laboratory of Fine Chemicals, PSU-DUT Joint Center for Energy Research, School of Chemical Engineering, Dalian University of Technology, Dalian 116024, China; Email: [niexiaowa@dlut.edu.cn](mailto:niexiaowa@dlut.edu.cn)

Xiaopeng Han – School of Materials Science and Engineering, Tianjin Key Laboratory of Composite and Functional Materials, Key Laboratory of Advanced Ceramics and Machining Technology (Ministry of Education), Tianjin University, Tianjin 300072, China; [0000-0002-7557-7133](https://orcid.org/0000-0002-7557-7133); Email: [xphan@tju.edu.cn](mailto:xphan@tju.edu.cn)

Xinwen Guo – State Key Laboratory of Fine Chemicals, PSU-DUT Joint Center for Energy Research, School of Chemical Engineering, Dalian University of Technology, Dalian 116024, China; Email: [guoxw@dlut.edu.cn](mailto:guoxw@dlut.edu.cn)

**Authors**

**Haozhi Wang** – State Key Laboratory of Fine Chemicals, PSU-DUT Joint Center for Energy Research, School of Chemical Engineering, Dalian University of Technology, Dalian 116024, China; Joint School of National University of Singapore and Tianjin University, International Campus of Tianjin University, Fuzhou 350207, China; School of Materials Science and Engineering, Tianjin Key Laboratory of Composite and Functional Materials, Key Laboratory of Advanced Ceramics and Machining Technology (Ministry of Education), Tianjin University, Tianjin 300072, China

**Yuan Liu** – School of Materials Science and Engineering, Tianjin Key Laboratory of Composite and Functional Materials, Key Laboratory of Advanced Ceramics and Machining Technology (Ministry of Education), Tianjin University, Tianjin 300072, China

**Michael J. Janik** – EMS Energy Institute, PSU-DUT Joint Center for Energy Research, and Department of Energy & Mineral Engineering, Pennsylvania State University, University Park, Pennsylvania 16802, United States;  [orcid.org/0000-0001-9975-0650](https://orcid.org/0000-0001-9975-0650)

**Yida Deng** – School of Materials Science and Engineering, Tianjin Key Laboratory of Composite and Functional Materials, Key Laboratory of Advanced Ceramics and Machining Technology (Ministry of Education), Tianjin University, Tianjin 300072, China;  [orcid.org/0000-0002-8890-552X](https://orcid.org/0000-0002-8890-552X)

**Wenbin Hu** – Joint School of National University of Singapore and Tianjin University, International Campus of Tianjin University, Fuzhou 350207, China; School of Materials Science and Engineering, Tianjin Key Laboratory of Composite and Functional Materials, Key Laboratory of Advanced Ceramics and Machining Technology (Ministry of Education), Tianjin University, Tianjin 300072, China

**Chunshan Song** – State Key Laboratory of Fine Chemicals, PSU-DUT Joint Center for Energy Research, School of Chemical Engineering, Dalian University of Technology, Dalian 116024, China; Department of Chemistry, Faculty of Science, The Chinese University of Hong Kong, Shatin, NT 999077 Hong Kong, China;  [orcid.org/0000-0003-2344-9911](https://orcid.org/0000-0003-2344-9911)

Complete contact information is available at:

<https://pubs.acs.org/10.1021/acsami.2c07029>

**Notes**

The authors declare no competing financial interest.

**ACKNOWLEDGMENTS**

This work was financially supported by the National Key Research and Development Program of China (no. 2016YFB0600902), the National Natural Science Foundation of China (no. 21503027), and the Fundamental Research Funds for the Central Universities (DUT18LK20). We acknowledge the Supercomputing Center of the Dalian University of Technology and the National Super-Computer Center in Tianjin for providing the computational resources for this work.

**REFERENCES**

(1) Song, C. Global challenges and strategies for control, conversion and utilization of CO<sub>2</sub> for sustainable development involving energy, catalysis, adsorption and chemical processing. *Catal. Today* **2006**, *115*, 2–32.

(2) Saeidi, S.; Najari, S.; Fazlollahi, F.; Nikoo, M. K.; Sefidkon, F.; Klemeš, J. J.; Baxter, L. L. Mechanisms and kinetics of CO<sub>2</sub> hydrogenation to value-added products: A detailed review on current status and future trends. *Renewable Sustainable Energy Rev.* **2017**, *80*, 1292–1311.

(3) Li, W.; Wang, H.; Jiang, X.; Zhu, J.; Liu, Z.; Guo, X.; Song, C. A short review of recent advances in CO<sub>2</sub> hydrogenation to hydrocarbons over heterogeneous catalysts. *RSC Adv.* **2018**, *8*, 7651–7669.

(4) Nie, X.; Jiang, X.; Wang, H.; Luo, W.; Janik, M. J.; Chen, Y.; Guo, X.; Song, C. Mechanistic Understanding of Alloy Effect and Water Promotion for Pd-Cu Bimetallic Catalysts in CO<sub>2</sub> Hydrogenation to Methanol. *ACS Catal.* **2018**, *8*, 4873–4892.

(5) Albrecht, M.; Rodemerck, U.; Schneider, M.; Bröring, M.; Baabe, D.; Kondratenko, E. V. Unexpectedly efficient CO<sub>2</sub> hydrogenation to higher hydrocarbons over non-doped Fe<sub>2</sub>O<sub>3</sub>. *Appl. Catal., B* **2017**, *204*, 119–126.

(6) Jiang, X.; Nie, X.; Guo, X.; Song, C.; Chen, J. G. Recent Advances in Carbon Dioxide Hydrogenation to Methanol via Heterogeneous Catalysis. *Chem. Rev.* **2020**, *120*, 7984–8034.

(7) Zhou, H.; Chen, Z.; López, A. V.; López, E. D.; Lam, E.; Tsoukalou, A.; Willinger, E.; Kuznetsov, D. A.; Mance, D.; Kierzkowska, A.; Donat, F.; Abdala, P. M.; Comas-Vives, A.; Copéret, C.; Fedorov, A.; Müller, C. R. Engineering the Cu/Mo<sub>2</sub>CT<sub>x</sub> (MXene) interface to drive CO<sub>2</sub> hydrogenation to methanol. *Nat. Catal.* **2021**, *4*, 860–871.

(8) Zhao, X.; Wu, Z.; Fu, J.; Guo, J.; Kang, S. Designing FeO@graphite@C Nanocomposites Based on Humins as Efficient Catalysts for Reverse Water-Gas Shift. *ACS Appl. Mater. Interfaces* **2021**, *13*, 57100–57106.

(9) Guo, H.; Si, D. H.; Zhu, H. J.; Li, Q. X.; Huang, Y. B.; Cao, R. Ni Single-Atom Sites Supported on Carbon Aerogel for Highly Efficient Electroreduction of Carbon Dioxide with Industrial Current Densities. *eScience* **2022**, *2*, 295–303.

(10) Zhu, Z.; Li, Z.; Wang, J.; Li, R.; Chen, H.; Li, Y.; Chen, J. S.; Wu, R.; Wei, Z. Improving NiN<sub>x</sub> and Pyridinic N Active Sites with Space-Confining Pyrolysis for Effective CO<sub>2</sub> electroreduction. *eScience* **2022**, DOI: [10.1016/j.esci.2022.05.002](https://doi.org/10.1016/j.esci.2022.05.002).

(11) Li, Y.; Chan, S. H.; Sun, Q. Heterogeneous catalytic conversion of CO<sub>2</sub>: a comprehensive theoretical review. *Nanoscale* **2015**, *7*, 8663–8683.

(12) Satthawong, R.; Koizumi, N.; Song, C.; Prasassarakich, P. Light olefin synthesis from CO<sub>2</sub> hydrogenation over K-promoted Fe-Co bimetallic catalysts. *Catal. Today* **2015**, *251*, 34–40.

(13) Hu, S.; Liu, M.; Ding, F.; Song, C.; Zhang, G.; Guo, X. Hydrothermally stable MOFs for CO<sub>2</sub> hydrogenation over iron-based catalyst to light olefins. *J. CO<sub>2</sub> Util.* **2016**, *15*, 89–95.

(14) Liu, J.; Zhang, A.; Liu, M.; Hu, S.; Ding, F.; Song, C.; Guo, X. Fe-MOF-Derived Highly Active Catalysts for Carbon Dioxide Hydrogenation to Valuable Hydrocarbons. *J. CO<sub>2</sub> Util.* **2017**, *21*, 100–107.

(15) Satthawong, R.; Koizumi, N.; Song, C.; Prasassarakich, P. Bimetallic Fe-Co catalysts for CO<sub>2</sub> hydrogenation to higher hydrocarbons. *J. CO<sub>2</sub> Util.* **2013**, *3-4*, 102–106.

(16) Satthawong, R.; Koizumi, N.; Song, C.; Prasassarakich, P. Comparative Study on CO<sub>2</sub> Hydrogenation to Higher Hydrocarbons over Fe-Based Bimetallic Catalysts. *Top. Catal.* **2013**, *57*, 588–594.

(17) Liu, B.; Geng, S.; Zheng, J.; Jia, X.; Jiang, F.; Liu, X. Unravelling the New Roles of Na and Mn Promoter in CO<sub>2</sub> Hydrogenation over Fe<sub>3</sub>O<sub>4</sub>-Based Catalysts for Enhanced Selectivity to Light  $\alpha$ -Olefins. *ChemCatChem* **2018**, *10*, 4718–4732.

(18) Numpilai, T.; Witoon, T.; Chanlek, N.; Limphirat, W.; Bonura, G.; Chareonpanich, M.; Limtrakul, J. Structure-activity relationships of Fe-Co/K-Al<sub>2</sub>O<sub>3</sub> catalysts calcined at different temperatures for CO<sub>2</sub> hydrogenation to light olefins. *Appl. Catal., A* **2017**, *547*, 219–229.

(19) Boreriboon, N.; Jiang, X.; Song, C.; Prasassarakich, P. Fe-based bimetallic catalysts supported on TiO<sub>2</sub> for selective CO<sub>2</sub> hydrogenation to hydrocarbons. *J. CO<sub>2</sub> Util.* **2018**, *25*, 330–337.

(20) Amoyal, M.; Vidruk-Nehemya, R.; Landau, M. V.; Herskowitz, M. Effect of Potassium on the Active Phases of Fe Catalysts for

- Carbon Dioxide Conversion to Liquid Fuels Through Hydrogenation. *J. Catal.* **2017**, *348*, 29–39.
- (21) Visconti, C. G.; Martinelli, M.; Falbo, L.; Fratalocchi, L.; Lietti, L. CO<sub>2</sub> hydrogenation to hydrocarbons over Co and Fe-based Fischer-Tropsch catalysts. *Catal. Today* **2016**, *277*, 161–170.
- (22) Zhu, J.; Wang, P.; Zhang, X.; Zhang, G.; Li, R.; Li, W.; Senftle, T. P.; Liu, W.; Wang, J.; Wang, Y.; Zhang, A.; Fu, Q.; Song, C.; Guo, X. Dynamic Structural Evolution of Iron Catalysts Involving Competitive Oxidation and Carburization During CO<sub>2</sub> Hydrogenation. *Sci. Adv.* **2022**, *8*, 3629.
- (23) Liu, J.; Zhang, G.; Jiang, X.; Wang, J.; Song, C.; Guo, X. Insight into the role of Fe<sub>5</sub>C<sub>2</sub> in CO<sub>2</sub> catalytic hydrogenation to hydrocarbons. *Catal. Today* **2021**, *371*, 162–170.
- (24) Elishav, O.; Shener, Y.; Beilin, V.; Landau, M. V.; Herskowitz, M.; Shter, G. E.; Grader, G. S. Electrospun Fe-Al-O Nanobelts for Selective CO<sub>2</sub> Hydrogenation to Light Olefins. *ACS Appl. Mater. Interfaces* **2020**, *12*, 24855–24867.
- (25) Wu, T.; Lin, J.; Cheng, Y.; Tian, J.; Wang, S.; Xie, S.; Pei, Y.; Yan, S.; Qiao, M.; Xu, H.; Zong, B. Porous Graphene-Confining Fe-K as Highly Efficient Catalyst for CO<sub>2</sub> Direct Hydrogenation to Light Olefins. *ACS Appl. Mater. Interfaces* **2018**, *10*, 23439–23443.
- (26) Zhang, Y.; Fu, D.; Liu, X.; Zhang, Z.; Zhang, C.; Shi, B.; Xu, J.; Han, Y. F. Operando Spectroscopic Study of Dynamic Structure of Iron Oxide Catalysts during CO<sub>2</sub> Hydrogenation. *ChemCatChem* **2018**, *10*, 1272–1276.
- (27) Liu, J.; Zhang, A.; Jiang, X.; Liu, M.; Sun, Y.; Song, C.; Guo, X. Selective CO<sub>2</sub> Hydrogenation to Hydrocarbons on Cu-Promoted Fe-Based Catalysts: Dependence on Cu-Fe Interaction. *ACS Sustainable Chem. Eng.* **2018**, *6*, 10182–10190.
- (28) Zhang, Q.; Pastor-Pérez, L.; Wang, Q.; Ramirez Reina, T. Conversion of CO<sub>2</sub> to added value products via rWGS using Fe-promoted catalysts: Carbide, metallic Fe or a mixture? *J. Energy Chem.* **2022**, *66*, 635–646.
- (29) Wang, S.; Ji, Y.; Liu, X.; Yan, S.; Xie, S.; Pei, Y.; Li, H.; Qiao, M.; Zong, B. Potassium as a Versatile Promoter to Tailor the Distribution of the Olefins in CO<sub>2</sub> Hydrogenation over Iron-Based Catalyst. *ChemCatChem* **2022**, *14*, 202101535.
- (30) Nie, X.; Han, G.; Song, C.; Guo, X. Computational identification of facet-dependent CO<sub>2</sub> initial activation and hydrogenation over iron carbide catalyst. *J. CO<sub>2</sub> Util.* **2022**, *59*, 101967.
- (31) Yang, C.; Zhao, H.; Hou, Y.; Ma, D. Fe<sub>5</sub>C<sub>2</sub> Nanoparticles: A Facile Bromide-Induced Synthesis and as an Active Phase for Fischer-Tropsch Synthesis. *J. Am. Chem. Soc.* **2012**, *134*, 15814–15821.
- (32) Tian, X.; Wang, T.; Yang, Y.; Li, Y. W.; Wang, J.; Jiao, H. Surface Morphology of Cu Adsorption on Different Terminations of the Hägg Iron Carbide ( $\chi$ -Fe<sub>5</sub>C<sub>2</sub>) Phase. *J. Phys. Chem. C* **2015**, *119*, 7371–7385.
- (33) Malina, O.; Jakubec, P.; Kašlik, J.; Tuček, J.; Zbořil, R. A simple high-yield synthesis of high-purity Hägg carbide ( $\chi$ -Fe<sub>5</sub>C<sub>2</sub>) nanoparticles with extraordinary electrochemical properties. *Nanoscale* **2017**, *9*, 10440–10446.
- (34) Yang, C.; Zhao, B.; Gao, R.; Yao, S.; Zhai, P.; Li, S.; Yu, J.; Hou, Y.; Ma, D. Construction of Synergistic Fe<sub>5</sub>C<sub>2</sub>/Co Heterostructured Nanoparticles as an Enhanced Low Temperature Fischer-Tropsch Synthesis Catalyst. *ACS Catal.* **2017**, *7*, 5661–5667.
- (35) Pham, T. H.; Duan, X.; Qian, G.; Zhou, X.; Chen, D. CO Activation Pathways of Fischer-Tropsch Synthesis on  $\chi$ -Fe<sub>5</sub>C<sub>2</sub> (510): Direct versus Hydrogen-Assisted CO Dissociation. *J. Phys. Chem. C* **2014**, *118*, 10170–10176.
- (36) Chen, B.; Wang, D.; Duan, X.; Liu, W.; Li, Y.; Qian, G.; Yuan, W.; Holmen, A.; Zhou, X.; Chen, D. Charge-Tuned CO Activation over a  $\chi$ -Fe<sub>5</sub>C<sub>2</sub> Fischer-Tropsch Catalyst. *ACS Catal.* **2018**, *8*, 2709–2714.
- (37) Pham, T. H.; Qi, Y.; Yang, J.; Duan, X.; Qian, G.; Zhou, X.; Chen, D.; Yuan, W. Insights into Hägg Iron-Carbide-Catalyzed Fischer-Tropsch Synthesis: Suppression of CH<sub>4</sub> Formation and Enhancement of C-C Coupling on  $\chi$ -Fe<sub>5</sub>C<sub>2</sub> (510). *ACS Catal.* **2015**, *5*, 2203–2208.
- (38) Lu, Y.; Zhang, R.; Cao, B.; Ge, B.; Tao, F.; Shan, J.; Nguyen, L.; Bao, Z.; Wu, T.; Pote, J. W.; Wang, B.; Yu, F. Elucidating the Copper-Hägg Iron Carbide Synergistic Interactions for Selective CO Hydrogenation to Higher Alcohols. *ACS Catal.* **2017**, *7*, 5500–5512.
- (39) Zhao, S.; Liu, X. W.; Huo, C. F.; Li, Y. W.; Wang, J.; Jiao, H. Potassium promotion on CO hydrogenation on the  $\chi$ -Fe<sub>5</sub>C<sub>2</sub> (111) surface with carbon vacancy. *Appl. Catal., A* **2017**, *534*, 22–29.
- (40) Kresse, G.; Furthmüller, J. Efficient Iterative Schemes for Ab Initio Total-Energy Calculations using a Plane-Wave Basis Set. *Phys. Rev. B: Condens. Matter Mater. Phys.* **1996**, *54*, 11169–11186.
- (41) Kresse, G.; Hafner, J. Ab initiomolecular dynamics for open-shell transition metals. *Phys. Rev. B: Condens. Matter Mater. Phys.* **1993**, *48*, 13115–13118.
- (42) Kresse, G.; Hafner, J. Ab initiomolecular dynamics for liquid metals. *Phys. Rev. B: Condens. Matter Mater. Phys.* **1993**, *47*, 558–561.
- (43) Blöchl, P. E. Projector Augmented-Wave Method. *Phys. Rev. B: Condens. Matter Mater. Phys.* **1994**, *50*, 17953–17979.
- (44) Kresse, G.; Joubert, D. From Ultrasoft Pseudopotentials to the Projector Augmented-Wave Method. *Phys. Rev. B: Condens. Matter Mater. Phys.* **1999**, *59*, 1758–1775.
- (45) Perdew, J. P.; Burke, K.; Ernzerhof, M. Generalized Gradient Approximation Made Simple. *Phys. Rev. Lett.* **1996**, *77*, 3865–3868.
- (46) Henkelman, G.; Uberuaga, B. P.; Jónsson, H. A Climbing Image Nudged Elastic Band Method for Finding Saddle Points and Minimum Energy Paths. *J. Chem. Phys.* **2000**, *113*, 9901–9904.
- (47) Henkelman, G.; Arnaldsson, A.; Jónsson, H. A Fast and Robust Algorithm for Bader Decomposition of Charge Density. *Comp. Mater. Sci.* **2006**, *36*, 354–360.
- (48) Chorkendorff, I.; Niemantsverdriet, J. W. *Concepts of Modern Catalysis and Kinetics*; WileyVCH: Weinheim, Germany, 2003; Vol. 8, p 7
- (49) McQuarrie, D. A.; Simon, J. D. Physical Chemistry: A Molecular Approach. *J. Chem. Educ.* **1998**, *75*, 545.
- (50) Choksi, T.; Greeley, J. Partial Oxidation of Methanol on MoO<sub>3</sub> (010): A DFT and Microkinetic Study. *ACS Catal.* **2016**, *6*, 7260–7277.
- (51) Wang, H.; Nie, X.; Chen, Y.; Guo, X.; Song, C. Facet effect on CO<sub>2</sub> adsorption, dissociation and hydrogenation over Fe catalysts: Insight from DFT. *J. CO<sub>2</sub> Util.* **2018**, *26*, 160–170.
- (52) Wang, H.; Nie, X.; Guo, X.; Song, C. A computational study of adsorption and activation of CO<sub>2</sub> and H<sub>2</sub> over Fe(1 0 0) surface. *J. CO<sub>2</sub> Util.* **2016**, *15*, 107–114.
- (53) Nie, X.; Meng, L.; Wang, H.; Chen, Y.; Guo, X.; Song, C. DFT insight into the effect of potassium on the adsorption, activation and dissociation of CO<sub>2</sub> over Fe-based catalysts. *Phys. Chem. Chem. Phys.* **2018**, *20*, 14694–14707.
- (54) Rodriguez, J. A.; Liu, P.; Stacchiola, D. J.; Senanayake, S. D.; White, M. G.; Chen, J. G. Hydrogenation of CO<sub>2</sub> to Methanol: Importance of Metal-Oxide and Metal-Carbide Interfaces in the Activation of CO<sub>2</sub>. *ACS Catal.* **2015**, *5*, 6696–6706.
- (55) Kim, Y.; Trung, T. S. B.; Yang, S.; Kim, S.; Lee, H. Mechanism of the Surface Hydrogen Induced Conversion of CO<sub>2</sub> to Methanol at Cu(111) Step Sites. *ACS Catal.* **2016**, *6*, 1037–1044.
- (56) Wu, P.; Yang, B. Significance of Surface Formate Coverage on the Reaction Kinetics of Methanol Synthesis from CO<sub>2</sub> Hydrogenation over Cu. *ACS Catal.* **2017**, *7*, 7187–7195.
- (57) Maintz, S.; Deringer, V. L.; Tchougréeff, A. L.; Dronskowski, R. LOBSTER: A Tool to Extract Chemical Bonding from Plane-Wave Based DFT. *J. Comput. Chem.* **2016**, *37*, 1030–1035.
- (58) Deringer, V. L.; Tchougréeff, A. L.; Dronskowski, R. Crystal Orbital Hamilton Population (COHP) Analysis as Projected from Plane-Wave Basis Sets. *J. Phys. Chem. A* **2011**, *115*, 5461–5466.
- (59) Liu, J.; Sun, Y.; Jiang, X.; Zhang, A.; Song, C.; Guo, X. Pyrolyzing ZIF-8 to N-doped porous carbon facilitated by iron and potassium for CO<sub>2</sub> hydrogenation to value-added hydrocarbons. *J. CO<sub>2</sub> Util.* **2018**, *25*, 120–127.
- (60) Nie, X.; Wang, H.; Janik, M. J.; Chen, Y.; Guo, X.; Song, C. Mechanistic Insight into C-C Coupling over Fe-Cu Bimetallic

- Catalysts in CO<sub>2</sub> Hydrogenation. *J. Phys. Chem. C* **2017**, *121*, 13164–13174.
- (61) Liu, J.; Zhang, A.; Jiang, X.; Liu, M.; Zhu, J.; Song, C.; Guo, X. Direct Transformation of Carbon Dioxide to Value-Added Hydrocarbons by Physical Mixtures of Fe<sub>5</sub>C<sub>2</sub> and K-Modified Al<sub>2</sub>O<sub>3</sub>. *Ind. Eng. Chem. Res.* **2018**, *57*, 9120–9126.
- (62) Bordet, A.; Asensio, J. M.; Soulantica, K.; Chaudret, B. Enhancement of Carbon Oxides Hydrogenation on Iron-Based Nanoparticles by In-Situ Water Removal. *ChemCatChem* **2018**, *10*, 4047–4051.
- (63) Campbell, C. T. Finding the Rate-Determining Step in a Mechanism. *J. Catal.* **2001**, *204*, 520–524.
- (64) Wolcott, C. A.; Medford, A. J.; Studt, F.; Campbell, C. T. Degree of Rate Control Approach to Computational Catalyst Screening. *J. Catal.* **2015**, *330*, 197–207.
- (65) Zhu, J.; Wang, P.; Zhang, X. B.; Zhang, G. H.; Li, R. T.; Li, W. H. Dynamic Structural Evolution of Iron Catalysts Involving Competitive Oxidation and Carburization during CO<sub>2</sub> Hydrogenation. *Sci. Adv.* **2022**, *8*, 3629.
- (66) Boreriboon, N.; Jiang, X.; Song, C.; Prasassarakich, P. Higher Hydrocarbons Synthesis from CO<sub>2</sub> Hydrogenation Over K- and La-Promoted Fe-Cu/TiO<sub>2</sub> Catalysts. *Top. Catal.* **2018**, *61*, 1551–1562.
- (67) Niu, L.; Liu, X.; Liu, J.; Liu, X.; Wen, X.; Yang, Y.; Xu, J.; Li, Y. Tuning carburization behaviors of metallic iron catalysts with potassium promoter and CO/syngas/C<sub>2</sub>H<sub>4</sub>/C<sub>2</sub>H<sub>2</sub> gases. *J. Catal.* **2019**, *371*, 333–345.
- (68) Wang, Y. X.; Wang, G. C. A Systematic Theoretical Study of Water Gas Shift Reaction on Cu(111) and Cu(110): Potassium Effect. *ACS Catal.* **2019**, *9*, 2261–2274.
- (69) Wang, Y. X.; Wang, G. C. Water Dissociation on Clean and Potassium Preadsorbed Transition Metals: A Systematic Theoretical Study. *J. Phys. Chem. C* **2018**, *122*, 15474–15484.
- (70) Wang, Y. X.; Wang, G. C. Water dissociation on K<sub>2</sub>O-pre-adsorbed transition metals: a systematic theoretical study. *Phys. Chem. Chem. Phys.* **2018**, *20*, 19850–19859.

## □ Recommended by ACS

### Tandem CO<sub>2</sub> Valorization and Ethane Dehydrogenation: Elucidating the Nature of Highly Selective Iron Oxide Active Sites

Maria Tasioula, Angeliki A. Lemonidou, et al.

JANUARY 26, 2023

ACS CATALYSIS

READ ↗

### Oxidative Dehydrogenation of Ethane with CO<sub>2</sub> over the Fe-Co/Al<sub>2</sub>O<sub>3</sub> Catalyst: Experimental Data Assisted AI Models for Prediction of Ethylene Yield

Sangeetha Povari, Sumana Chenna, et al.

FEBRUARY 02, 2023

INDUSTRIAL & ENGINEERING CHEMISTRY RESEARCH

READ ↗

### Evolution of Active Oxygen Species Originating from O<sub>2</sub> Cleavage over Fe-FER for Application in Methane Oxidation

Kinga Mlekodaj, Ewyta Tabor, et al.

FEBRUARY 21, 2023

ACS CATALYSIS

READ ↗

### Descriptors Affecting Methane Selectivity in CO<sub>2</sub> Hydrogenation over Unpromoted Bulk Iron(III)-Based Catalysts

Andrey S. Skrypnik, Evgenii V. Kondratenko, et al.

SEPTEMBER 02, 2022

ACS CATALYSIS

READ ↗

Get More Suggestions >